

Radio Interferometric Studies of Cool Evolved Stellar Winds

A dissertation submitted to the University of Dublin
for the degree of Doctor of Philosophy

Eamon O'Gorman

Supervisor: Prof. Graham M. Harper
Trinity College Dublin, September 2013

SCHOOL OF PHYSICS
UNIVERSITY OF DUBLIN
TRINITY COLLEGE



Declaration

I declare that this thesis has not been submitted as an exercise for a degree at this or any other university and it is entirely my own work.

I agree to deposit this thesis in the University's open access institutional repository or allow the library to do so on my behalf, subject to Irish Copyright Legislation and Trinity College Library conditions of use and acknowledgement.

Name: Eamon O'Gorman

Signature: **Date:**

Summary

Mass-loss becomes significant for most stars as they approach the end of their lives and become either red giants or red supergiants. This continuous mass-loss, which occurs in the form of a relatively dense and slow-moving wind, can have a significant impact on the evolution of gas and dust in galaxies, on surrounding planets, and indeed on the very evolution of the star itself. Despite the importance of this phenomenon and decades of study, the fundamental mechanisms responsible for producing these winds remain unknown. The main reason for this is due to our lack of understanding of the dynamics and thermodynamics of the stellar outflow environment. Isolated giants and supergiants do not contain the expected additional complexities encountered by binaries, making them ideal targets for understanding the nature of these outflows. Traditionally, observations have provided only limited disk-averaged information about the outflow environments of these stars, making it difficult to infer the outflow properties. However, the latest suite of radio interferometers now have the capability to provide essential spatial information on these outflow environments.

This thesis first presents the results of a radio interferometric study into the dynamics of the two unique flows in the circumstellar environment of the M2 red supergiant, Betelgeuse. The Combined Array for Research in Millimeter-wave Astronomy (CARMA) was used in multiple configurations to observe the CO($J = 2 - 1$) emission line allowing spatial scales as small as $0''.9$ ($\sim 40 R_\star$) to be traced over a $32''$ ($\sim 1500 R_\star$) field of view. The outer flow known as S2, was found to have outflow velocities of -15.4 and $+13.2 \text{ km s}^{-1}$ with respect to the stellar rest frame and extend out to $17''$, while the inner

flow known as S1, was found to have outflow velocities of -9.0 and +10.6 km s⁻¹ and extend out to between 4 – 6''. Both flows were found to be inhomogeneous down to the resolution limit, but when azimuthally averaged, their intensity falloff was found to be consistent with an optically thin, spherically symmetric, constant velocity outflow. High resolution multi-epoch centimeter continuum observations of Betelgeuse which probe its inner atmosphere ($< 10 R_\star$) are also presented. The radio flux density is found to vary on time scales of $\lesssim 14$ months at all wavelengths, and again evidence for inhomogeneities in the outflow is found.

Karl G. Jansky Very Large Array (VLA) multi-wavelength centimeter observations of two non-dusty, non-pulsating K spectral-type red giants, Arcturus and Aldebaran, were also analyzed. Detections at 10 cm (3.0 GHz: S-band) and 20 cm (1.5 GHz: L-band) represent the first isolated luminosity class III red giants to be detected at these long wavelengths. These thermal continuum observations provide a snapshot of the different stellar atmospheric layers and are independent of any long-term variability. The long wavelength data sample Arcturus' outer atmosphere where the wind velocity is approaching its terminal value and the ionization balance is becoming *frozen-in*. For Aldebaran, the data samples its inner atmosphere where the wind is still accelerating. Our data is in conflict with published semi-empirical models based on ultraviolet data. Spectral indices are used to discuss the possible properties of the stellar atmospheres. Evidence for a rapidly cooling wind in the case of Arcturus is found and a new analytical wind model is developed for this star. This model is used as the basis to compute a thermal energy balance of Arcturus' outflow by investigating the various heating and cooling processes that control its thermal structure. The analysis focuses on distances between 1.2 and $10 R_\star$, and includes the wind acceleration zone. We find that a substantial additional heating mechanism is required to maintain the inner thermal structure of the outflow.

*For Mum and Dad,
a constant source of inspiration and guidance.*

Acknowledgements

I am immensely grateful to my supervisor Graham Harper. His enthusiasm, dedication, patience, and encouragement, have been a huge help to me over the past four years. His knowledge and passion for the subject is beyond belief.

I would like to thank Joanna Brown, Alex Brown, and Anita Richards, for their help and advice with the data analysis aspects of this thesis.

I would also like to thank all past and present members of the Astrophysics Research Group. It has been great getting to know everybody and you have made the last four years an unforgettable experience.

A huge thanks to Sarah for proof reading this thesis, to Alex for providing me with a roof over my head during the write-up, and to Claire for keeping me motivated all the way from Brussels. Finally and most importantly, I would like to thank Mum and Dad for everything.

List of Publications

Refereed

1. **O'Gorman, E.**, Harper, G. M., Brown, A., Brown, A., Drake, S., and Richards, A. M. S.
“Multi-wavelength Radio Continuum Emission Studies of Dust-free Red Giants”
The Astronomical Journal, 146, 98 (2013)
2. Richards, A. M. S., Davis, R. J., Decin, L., Etoka, S., Harper, G. M., Lim, J. J., Garrington, S. T., Gray, M. D., McDonald, I., **O'Gorman, E.**, Wittkowski, M.
“e-MERLIN resolves Betelgeuse at wavelength 5 cm”
Monthly Notices of the Royal Astronomical Society Letters, 432, L61 (2013)
3. **O'Gorman, E.**, Harper, G. M., Brown, J. M., Brown, A., Redfield, S., Richter, M. J., and Requena-Torres, M. A.
“CARMA CO($J = 2 - 1$) Observations of the Circumstellar Envelope of Betelgeuse”
The Astronomical Journal, 144, 36 (2012)
4. Sada, P. V., Deming, D., Jennings, D. E., Jackson, B. K., Hamilton, C. M., Fraine, J., Peterson, S. W., Haase, F., Bays, K., Lunsford, A., and **O'Gorman, E.**
“Extrasolar Planet Transits Observed at Kitt Peak National Observatory”
Publications of the Astronomical Society of the Pacific, 124, 212 (2012)

-
5. Sada, P. V., Deming, D., Jackson, B. K., Jennings, D. E., Peterson, S. W., Haase, F., Bays, K., **O'Gorman, E.**, and Lundsford, A.
“Recent Transits of the Super-Earth Exoplanet GJ 1214b”
The Astrophysical Journal Letters, 720, L215 (2010)

Non-refereed

1. **O'Gorman, E.**, & Harper, G. M.
“What is Heating Arcturus’ Wind?”,
Proceedings of the 16th Cambridge Workshop on Cool Stars, Stellar Systems and the Sun. Astronomical Society of the Pacific Conference Series, 448, 691 (2011)

Contents

List of Publications	vii
List of Figures	xi
List of Tables	xii
1 Multi-wavelength Radio Emission Study of Betelgeuse’s Extended Atmosphere	1
1.1 CO molecules in the CSE of Betelgeuse	2
1.2 Adopted Radial Velocity	5
1.3 CARMA CO($J = 2 - 1$) Spectra	6
1.4 Individual Configuration Image Cubes	11
1.5 Multi-configuration Image Cube Inspection	12
1.6 Spatial Extent of S2	13
1.7 Intensity distribution of CO	15
1.8 Spatial Extent of S1	18
1.9 Continuum Flux Densities	19
1.10 Higher CO rotational lines	21
1.11 CARMA CO observations in Context	25
1.12 e-Merlin 6 cm Results	27
1.13 VLA-Pie Town Maps vs e-MERLIN	32
1.14 Long Term Radio Variability and Thermal Structure	34
1.15 0.7 cm VLA-Pie Town Maps	37
1.16 VLA, VLA-Pie, e-MERLIN: Putting it all together	38
A List of Abbreviations Used in this Thesis.	41

CONTENTS

References	43
-------------------	-----------

List of Figures

1.1	Bernat (1979) CO line profile showing two sharp line cores	3
1.2	Previous CO($J = 2 - 1$) rotational emission line profiles	4
1.3	Radial velocity data and model for α Ori	6
1.4	Spectra for each CARMA configuration	7
1.5	Spectra extracted over various regions	10
1.6	Geometry of a spherical symmetric flow	14
1.7	S2 radius as a function of channel velocity	15
1.8	Surface brightness vs. projected radius	17
1.9	CARMA maps of the inner S1 flow	19
1.10	CO rotational emission lines from the CSE of Betelgeuse	23
1.11	SiO rotational emission line from the CSE of Betelgeuse	24
1.12	First e-MERLIN results for Betelgeuse	28
1.13	Predicted position of Betelgeuse on 2012 July	30
1.14	1-D model vs. e-MERLIN observations	31
1.15	Radio flux density variation of Betelgeuse between 1996 → 2004 .	35
1.16	Atmospheric temperature profile between 1998 – 2013	36
1.17	Pie Town Q band images spanning six years	39

List of Tables

1.1	CARMA Continuum Fluxes at 230 GHz	20
1.2	Summary of the S1 and S2 Flow Properties	26
A.1	List of Abbreviations	41

1

Multi-wavelength Radio Emission Study of Betelgeuse’s Extended Atmosphere

The results from our multi-wavelength high spatial resolution study of Betelgeuse’s extended atmosphere are presented in this chapter. The majority of the chapter is based on the work of O’Gorman *et al.* (2012) and presents the results of our sub-arcsecond resolution study into the distribution and kinematics of $^{12}\text{C}^{16}\text{O}$ around Betelgeuse using the $^{12}\text{C}^{16}\text{O}(J = 2 - 1)$ rotational line as the main probe. The variation of the emission line profile with different CARMA array configurations provides us with a unique insight into the distribution and kinematics of the two previously known flows, S1 and S2, around Betelgeuse. We successfully image the star on spatial scales as small as $0''.9$ ($\sim 40 R_\star$) over a $32''$ ($\sim 1500 R_\star$) field of view and we discuss these radio maps in detail. We then compare these results to higher CO¹ rotational lines obtained with other instruments. We also present the recent findings of Richards *et al.* (2013) who image two distinct chromospheric features at centimeter wavelengths. These surprising findings motivated us to re-analyze archival VLA-Pie Town data to search for

¹Throughout this thesis, the term CO refers to the molecular isotopologue $^{12}\text{C}^{16}\text{O}$.

1.1 CO molecules in the CSE of Betelgeuse

these features at shorter wavelengths with comparable resolution, the results of which are presented at the end of the chapter.

1.1 CO molecules in the CSE of Betelgeuse

The CSE of Betelgeuse (α Ori) is a proving ground for ideas and theories of mass-loss from oxygen-rich M-type supergiants. Currently it is losing mass at a respectable rate $\sim 2 \times 10^{-6} M_{\odot} \text{ yr}^{-1}$ (Harper *et al.*, 2001), as it has been over the past ~ 1000 years. Most of the optically thin silicate dust lies beyond $\sim 46 R_{\star}$ (Danchi *et al.*, 1994) and therefore dust is unlikely to be responsible for the bulk mass-loss. This raises the important point that if the mass-loss from Betelgeuse is not a result of dust then perhaps the same mechanisms that are responsible might also be active in the more dusty later M-type supergiants. Radiation pressure on atoms and molecules is another potential contributing candidate as a mass-loss mechanism and so spatial and dynamical studies of molecules are a fruitful line of investigation, especially in relation to eventual formation of dust. Such studies also allow us to calculate the time scales on which certain mass-loss episodes have occurred, and these can then be compared to the time scales of potential mass-loss initiators such as convection or magnetic dynamo cycles.

Despite the initial reports of an enhancement of C abundance in its atmosphere (Spinrad & Vardya, 1966), Betelgeuse is now known to be an oxygen-rich star. The comprehensive study of CO and OH ro-vibrational bands by Lambert *et al.* (1984) found $\log_{10} \epsilon(\text{C}) = 8.4$ and $\log_{10} \epsilon(\text{O}) = 8.8$. For any species X

$$\log_{10} \epsilon(\text{X}) = \log_{10} (\text{X}/\text{H}) + 12, \quad (1.1)$$

which can be used to show O/C= 2.5. Lambert *et al.* (1984) also found $\log_{10} \epsilon(\text{N}) = 8.6$ which indicates a contamination of the atmosphere with C-N processed material. This is in agreement with the theoretical work of Lamb *et al.* (1976) who predict the dredging up of processed material by the deep convective envelope which a supergiant like Betelgeuse is expected to possess. Betelgeuse is unlikely to have undergone a second dredge-up of material that would cause small changes in the CNO abundances due to its mass being greater than the upper mass limit for a second dredge-up to occur (see Chapter ??). This second dredge-up is

1.1 CO molecules in the CSE of Betelgeuse

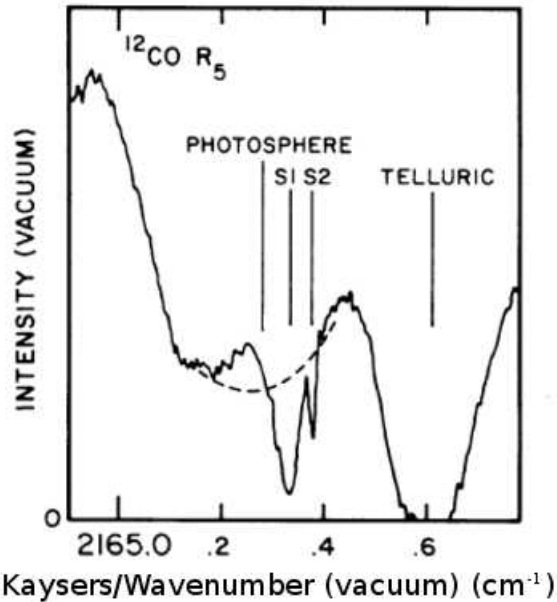


Figure 1.1: CO ro-vibrational fundamental line showing two sharp blueshifted absorption features originating from the expanding envelope (Bernat *et al.*, 1979). These two features became known as the S1 and S2 components of Betelgeuse’s outflow having outflow velocities of ~ 9 and $\sim 16 \text{ km s}^{-1}$, respectively. The units of the x-axis are in Kaysers, where $1 \text{ Kayser} = 1 \text{ cm}^{-1}$.

predicted to occur after He core exhaustion for stars below $8 - 10 M_{\odot}$ (Kaler *et al.*, 1978). The observed $^{12}\text{C}/^{13}\text{C}$ ratio, which is an indication of the history of nuclear processing and mixing in the interior of stars (Eggleton *et al.*, 2007; Pavlenko *et al.*, 2003), has consistently found to be between 6 and 7 in both the photosphere and CSE (Bernat *et al.*, 1979; Harris & Lambert, 1984; Hinkle *et al.*, 1976; Lambert *et al.*, 1974). These values are well below the predicted value of 20 (Charbonnel, 1995; Pavlenko *et al.*, 2003), which is expected for most lower mass red giant stars (e.g., Boothroyd & Sackmann, 1999).

The study of CO molecules in the CSE of Betelgeuse began with the detection of $4.6 \mu\text{m}$ ro-vibrational absorption lines of $^{12}\text{C}^{16}\text{O}$ and $^{13}\text{C}^{16}\text{O}$ by Bernat *et al.* (1979) who identified two absorption features shown in Figure 1.1, implying two distinct components within the overall outflow. One component, known as S1, has a Doppler shift of 9 km s^{-1} towards us with $T_{\text{exc}} \simeq 200_{-10}^{+50} \text{ K}$, $v_{\text{turb}} \simeq 4 \text{ km s}^{-1}$,

1.1 CO molecules in the CSE of Betelgeuse

and $N_{CO} = 4.7 \times 10^{17} \text{ cm}^{-2}$. The second faster component, known as S2, has a Doppler shift of 16 km s^{-1} towards us with $T_{\text{exc}} \simeq 70 \pm 10 \text{ K}$, $v_{\text{turb}} \simeq 1 \text{ km s}^{-1}$, and $N_{CO} = 1.2 \times 10^{16} \text{ cm}^{-2}$. Bernat *et al.* (1979) noted that a simple assumption of the dust and gas being in thermal equilibrium would infer that the S1 and S2 components have a spatial extent of 4 and $55''$ respectively, using the dust model of Tsuji (1979). The S1 feature with its higher column density was well known from atomic absorption line studies (e.g. Weymann, 1962) and both features had been detected in high spectral resolution atomic Na and K absorption profiles (Goldberg *et al.*, 1975).

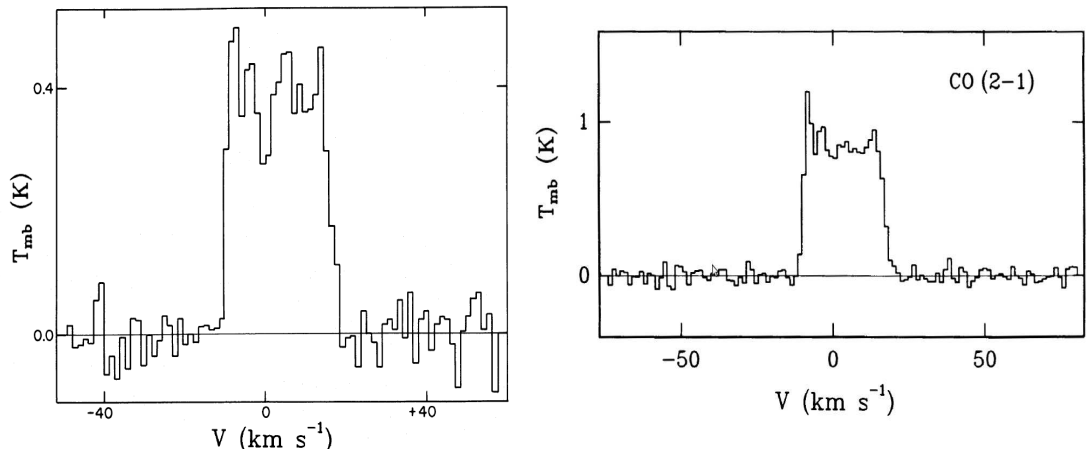


Figure 1.2: Previous single dish CO($J = 2 - 1$) rotational emission line profiles of Betelgeuse. *Left:* Huggins (1987) line profile using a HPBW of $32''$. *Right:* The line of Huggins *et al.* (1994) looks very similar even using a smaller HPBW in conflict with the findings of Huggins (1987). Velocities are plotted in the local standard of rest (LSR) frame.

CO was first detected at radio wavelengths by Knapp *et al.* (1980) who presented a low S/N spectrum of the $J = 2 - 1$ rotational emission line at 230 GHz. They used a single dish antenna with a HPBW of $\sim 30''$ and detected one component expanding at 15 km s^{-1} . They assumed this component to be the S2 component detected by Bernat *et al.* (1979) and by assuming that they had resolved a flat top profile, predicted that its spatial extent did not exceed $10''$. The weaker CO($J = 1 - 0$) line was tentatively detected by Knapp & Morris (1985) with a 7 m dish which had a HPBW of $100''$. Huggins (1987) presented a higher

1.2 Adopted Radial Velocity

S/N CO($J = 2 - 1$) profile that was obtained with a HPBW of $32''$ and is shown in Figure 1.2. By comparing the $(2 - 1)/(1 - 0)$ line intensities they found some evidence for an S2 radius of $\sim 16''$. However, a 30 m IRAM $J = 2 - 1$ line profile was later presented by Huggins *et al.* (1994) and as can be seen in Figure 1.2 looks remarkably similar, even though it was observed with a smaller $12''$ HPBW. The profile did not show the horned wing signature expected if it had been resolved as discussed in Chapter 1, apparently in conflict with the previous S2 radius estimate. These single dish line profiles also showed no obvious signature of the slower S1 shell and so questions remained about the spatial extent of these two distinct outflow components in the CSE of Betelgeuse. A sensitive high spatial resolution study of its atmosphere was needed to untangle this puzzling evidence.

1.2 Adopted Radial Velocity

Before we discuss the CO($J = 2 - 1$) spectra obtained from our multi-configuration CARMA observations, which are summarized in Chapter 3, we begin by explaining which radial velocity value v_{rad} , for Betelgeuse was adopted. An accurate value of v_{rad} is necessary when plotting the spectra of any star with respect to its center of mass rest frame, as we do for all spectra in this chapter. Plotting spectra in this frame of reference is intuitive as it allows the reader to immediately see the gas expansion velocity relative to the photosphere. A positive v_{rad} denotes recession (i.e., redshifted lines) while a negative v_{rad} denotes advancement (i.e., blueshifted lines).

Betelgeuse is a semi-regular variable and its radial velocity exhibits variability on time scales ranging from short 1.5 year periods as suggested by Stebbins & Huffer (1931) to longer 5.8 year periods (Smith *et al.*, 1989; Spencer Jones, 1928). Stothers & Leung (1971) interpreted the long period as being the convective turnover time of giant convection cells on the stellar surface while Dupree *et al.* (1990) attribute the shorter period with pulsation. Betelgeuse's radial velocity amplitudes are also known to vary by at least $\pm 3 \text{ km s}^{-1}$ (Smith *et al.*, 1989) making it difficult to determine a precise value for the stellar center of mass radial velocity. In Figure 1.3 we plot the radial velocity data and the corresponding model derived by Sanford (1933) which is based on observations spanning 1923

1.3 CARMA CO($J = 2 - 1$) Spectra

to 1931. We have also extrapolated the model back to show that it matches the earlier data of Bottlinger (1911) and Spencer Jones (1928) quite well, as shown in Figure 1.3. Goldberg (1984) has also shown that the model of Sanford (1933) can be extrapolated forward to give a reasonable fit to his measurements. In this study we adopt a heliocentric radial velocity of $+20.7 \text{ km s}^{-1}$; a value used by Weymann (1962) and Harper *et al.* (2008) and is based on the mean values of Spencer Jones (1928) and Sanford (1933) radial velocity models.

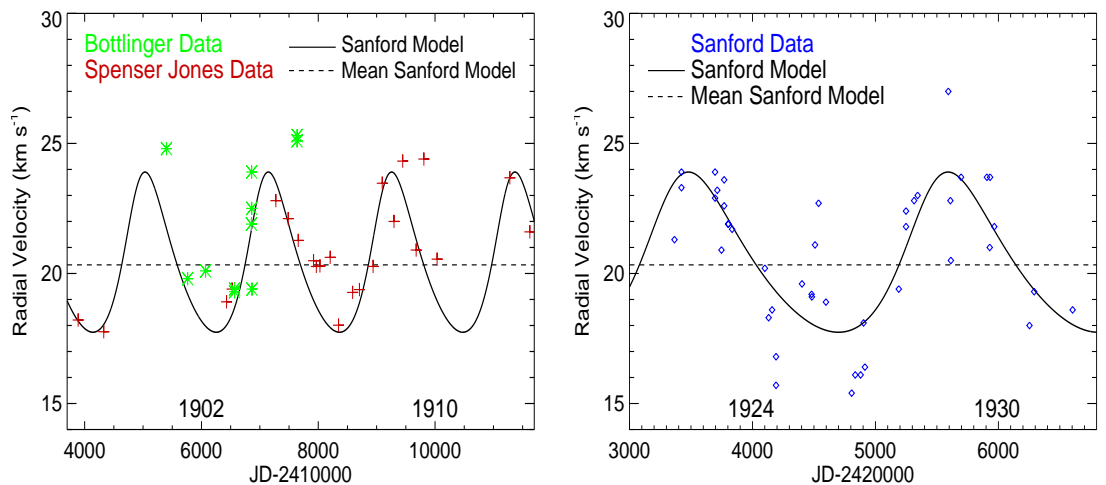


Figure 1.3: The radial velocity model of Sanford (1933) along with measurements from Bottlinger (1911), Spencer Jones (1928), and Sanford (1933) spanning the period 1897 – 1931. In this study we use $+20.7 \text{ km s}^{-1}$ which is the mean value from the models of Spencer Jones (1928) and Sanford (1933). The radial velocity amplitude variations of $\sim \pm 3 \text{ km s}^{-1}$ is clearly evident in these data.

1.3 CARMA CO($J = 2 - 1$) Spectra

The spectrum for each individual CARMA configuration image cube (which are composed of all the appropriate configuration tracks listed in Table ??) along with the multi-configuration image cube (which is composed of the entire data set spanning $\sim 2.5 \text{ yr}$) can be used to obtain information on the kinematics of the S1 and S2 flows. In particular, it is of interest to see how the CO($J = 2 - 1$) line profile changes, when observed with different array configurations, as each of these

1.3 CARMA CO($J = 2 - 1$) Spectra

will be sensitive to emission on different spatial scales. The spectra corresponding to the C, D, and E configuration image cubes are plotted in Figure 1.4 for both the high ($0.65 \text{ km s}^{-1} \text{ bin}^{-1}$) and low ($1.3 \text{ km s}^{-1} \text{ bin}^{-1}$) spectral resolution data and were obtained by integrating all emission within a circular area of radius $5''$ centered on the source. The high and low spectral resolution modes allow two independent sets of spectra to be measured for each observation and thus provide a good check on the data quality. The high resolution spectra (channel width = 0.65 km s^{-1}) give the best measure of the S1 and S2 flow kinematics and therefore all outflow velocities are derived from these spectra.

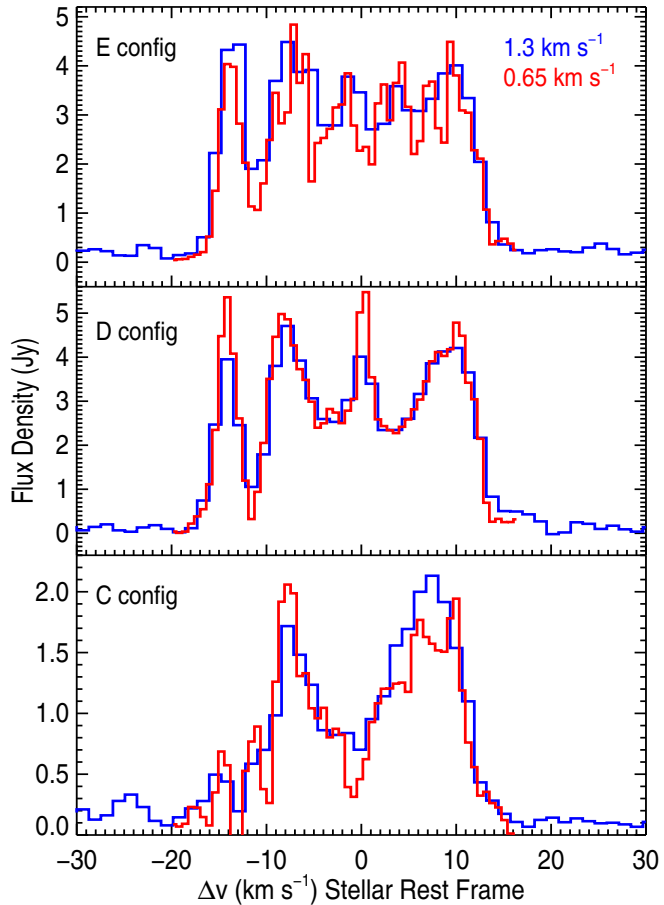


Figure 1.4: Spectra integrated over a radius of $5''$ for each array configuration image cube. The red and blue lines correspond to the high and low spectral resolution data respectively. The blueshifted emission component between -16.0 km s^{-1} and -10.0 km s^{-1} is almost resolved out in the C configuration image cube spectrum along with material with low absolute velocities.

1.3 CARMA CO($J = 2 - 1$) Spectra

The E configuration image cube spectrum has a total line width of 29.2 km s^{-1} and the low spectral resolution profile contains a steep blue wing emission feature between -16.0 km s^{-1} and -11 km s^{-1} and a more flat-topped feature between -10.3 km s^{-1} and $+13.2 \text{ km s}^{-1}$. This steep emission wing shows that the turbulence in the flow is less than or equal to the velocity bin size. The blue wing in the high resolution profile matches the lower resolution profile well but the remainder of the profile looks more complex than the flat-topped feature seen in the lower resolution profile. The line profile shape has been well documented by previous single dish observations (e.g., Figure 1.2) and, out of our three individual configuration spectra, we expect the most compact E configuration spectra to resemble these single dish measurements the closest due to its better sampling of the inner $u - v$ plane and consequent sensitivity to extended structures. This indeed turns out to be the case when we compare our three individual configuration spectra to those previous single dish profiles. The blue wing emission feature appears again in the D configuration spectrum at the same velocities as those in the E configuration spectrum but the remainder of the profile appears quite different. Between -10.3 km s^{-1} and $+13.2 \text{ km s}^{-1}$ the D configuration spectrum is dominated by a blue wing at $\sim -10.0 \text{ km s}^{-1}$, a red wing at $\sim +13.0 \text{ km s}^{-1}$ and an emission feature at $\sim 0 \text{ km s}^{-1}$. The large drop in emission at certain velocities in the D configuration spectrum is probably a result of the lower sensitivity to large scale structure in comparison to the E configuration as described in Table ??.

The line profile has a lower flux ($\sim 50\%$) in the high spatial resolution C configuration spectrum due to its lack of sensitivity to extended structure. Notably, the blueshifted emission feature located between -16.0 km s^{-1} and -11.0 km s^{-1} in the E and D configuration spectra is almost completely spatially filtered by the extended C configuration. This component of the line has previously been associated with the outer S2 flow (Huggins, 1987) and as the majority of it has been spatially filtered by our C configuration we expect even less contribution from the S2 flow at even lower absolute velocities. For the redshifted line emission we again expect the majority of the S2 contribution to be spatially filtered, so we conclude that most, if not all of the emission in the C configuration spectrum emanates from the inner S1 flow. The spectrum is double peaked with the blue and redshifted wings extending to $-9.0 \pm 0.7 \text{ km s}^{-1}$ and $+10.6 \pm 0.7 \text{ km s}^{-1}$.

1.3 CARMA CO($J = 2 - 1$) Spectra

respectively, and we define these as the outflow velocities of S1. As discussed in Chapter ?? the C configuration has a resolving out scale of $\sim 6''$ at 1.3 mm and so is not sensitive to angular scales larger than this. If the emission between -9.0 km s^{-1} and $+10.6 \text{ km s}^{-1}$ in the C configuration spectrum appeared as a flat topped profile then we could conclude that the S1 flow lies within a radius of $3''$ from the star. Clearly however, the profile has a more *horned* shaped appearance and so the lower absolute velocity components of this profile have been spatially filtered. We can therefore conclude that the radial extent of the S1 from the star is greater than $3''$. If we assume that the S1 flow would produce a 19.6 km s^{-1} wide top-hat line profile of 2 mJy were it not for the resolving out effects of the interferometer, its minimum integrated line flux is then

$$F_{\text{tot S1}} = F_\nu \times \left(\frac{\Delta v}{\lambda} \right) = 3.1 \times 10^{-19} \text{ W m}^{-2}. \quad (1.2)$$

To obtain the most robust value for the S2 outflow velocities we examine the high spectral resolution multi-configuration image cube spectrum which is composed of all tracks from all three configurations. It is worth stressing that by analyzing the multi-configuration image cube we make the assumption that the physical properties of all three components (i.e. α Ori, S1 and S2) have not changed over the total observation period (i.e. ~ 2.5 yr). The profile is found to have a total linewidth of $28.6 \pm 0.7 \text{ km s}^{-1}$, which is in good agreement with previous single dish observations of the line where values of $30.6 \pm 2.5 \text{ km s}^{-1}$ and 28.6 km s^{-1} were reported by Knapp *et al.* (1980) and Huggins (1987), respectively. The centroid velocity of the spectrum is $-1.1 \pm 0.7 \text{ km s}^{-1}$ ($v_{\text{lsr}} = 3.7 \pm 0.7 \text{ km s}^{-1}$) which again is in good agreement with Knapp *et al.* (1980) and Huggins (1987) values of $v_{\text{lsr}} = 3.0 \pm 2.5 \text{ km s}^{-1}$ and $v_{\text{lsr}} = 3.7 \pm 0.4 \text{ km s}^{-1}$, respectively. We use Equation 1.2 to find the integrated total line flux to be $1.5 \times 10^{-18} \text{ W m}^{-2}$, of which at least 20% emanates from the S1 flow.

The outflow velocities of S2 are $-15.4 \pm 0.7 \text{ km s}^{-1}$ and $+13.2 \pm 0.7 \text{ km s}^{-1}$ which, like the S1 flow, are slightly asymmetric but in the opposite sense. Note that the S1 and S2 outflow velocities are dependent on the adopted radial velocity of Betelgeuse. If for instance, we instead adopt a radial velocity of 21.9 km s^{-1} (Famaey *et al.*, 2005) then the S2 outflow velocities become even more

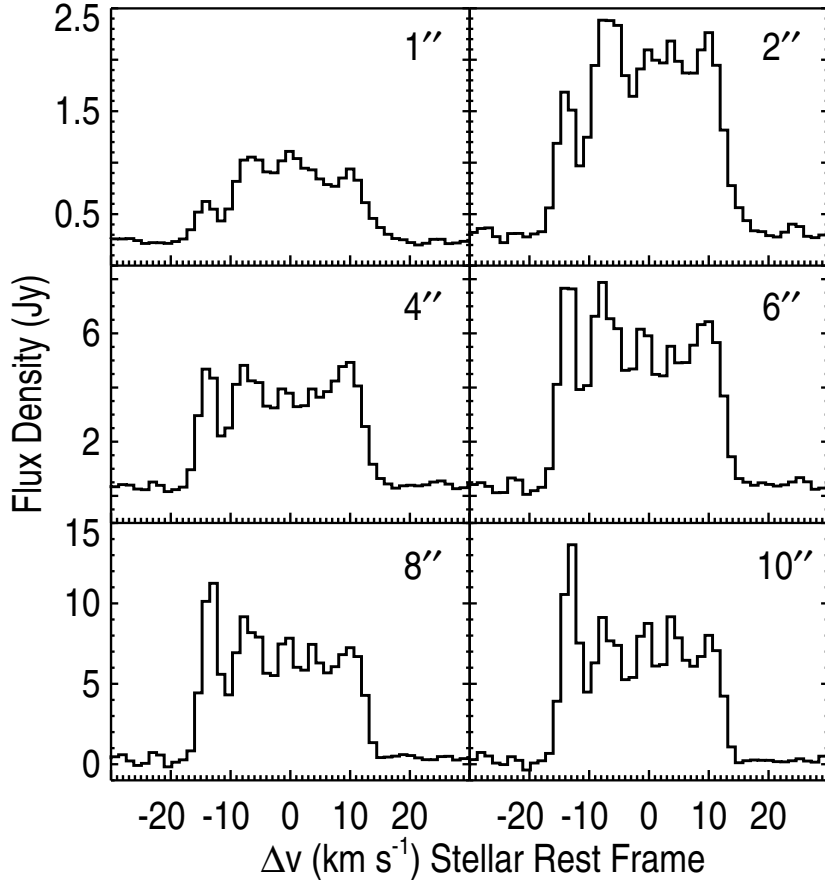


Figure 1.5: Spectral profiles of the low spectral resolution multi-configuration image cube for circular extraction areas of radius 1'', 2'', 4'', 6'', 8'', and 10''. The S/N of the line profile reduces at larger extraction areas as more noise is included from the outer more noisy regions of the channel maps.

asymmetric (-16.6 and +12.0 km s⁻¹) while the S1 outflow becomes less so (-10.2 and +9.4 km s⁻¹). Both S1 and S2 therefore cannot have spherically symmetric outflow velocities regardless of the adopted stellar radial velocity. Adopting a mass of $18 M_{\odot}$ (Meynet & Maeder, 2003) and a radius of $950 R_{\odot}$ (Harper *et al.*, 2008) then the escape velocity for Betelgeuse is 85 km s⁻¹ which is much greater than the S1 and S2 outflow velocities. This indicates that the majority of the stellar mass-loss mechanism's energy goes into lifting the CO molecules out of the gravitational potential and not into their outflow velocities. These outflow velocities are greater than the adiabatic hydrogen sound speed (i.e., $11.7\sqrt{10^{-4}T_e}$

1.4 Individual Configuration Image Cubes

km s^{-1}), which, if we assume that the gas temperature is the same as the excitation temperature, are 1.7 km s^{-1} and 1 km s^{-1} for S1 and S2 respectively.

The spectra in Figure 1.5 are taken from the low resolution multi-configuration image cube using circular extraction areas ranging in radius from $1''$ to $10''$ and demonstrates how the line profile changes over these different extraction areas. The most striking change in the line profile is the change in appearance of the extreme blue wing. At small extraction radii where we sample the most compact emission, the feature is weak in comparison to the rest of the line but becomes more dominant as we begin to sample more of the extended emission. This indicates that even the high absolute velocity components of the S2 flow have extended emission and this is why they are almost completely spatially filtered by CARMA’s C configuration. The large reduction of flux at -11 km s^{-1} suggests that there is more material moving towards the observer than at other lower absolute velocities, indicating a non-isotropic (or non-spherical) S2 flow. This suggests a more sheet like (flatter) structure rather than a spherical cap.

1.4 Individual Configuration Image Cubes

We created three image cubes for each configuration by concatenating all good tracks together per configuration. The gradual formation of a ring type structure as one goes from high absolute velocities to lower absolute velocities indicative of a shell was not seen in any of these three image cubes. An additional spatially unresolved source was clearly detected in a number of the D configuration image cube maps (both high and low spectral resolution). The component is present in five continuous channel maps between $\sim -4.0 \text{ km s}^{-1}$ and $+2.4 \text{ km s}^{-1}$ and is located $\sim 5''$ S-W of α Ori. Its peak emission lies at $\sim 0 \text{ km s}^{-1}$ and has a flux density of 1.8 mJy which is approximately 60% of the total source flux density at this velocity. The middle row in Figure ?? are two of these D configuration channel maps which clearly show this discrete source. The contour levels are set at the $4\sigma_{\text{rms}}$ level so the detection of the second source in the D configuration is significant. The corresponding channel maps in the E configuration image cube show extended emission out to $8''$ in the same S-W direction as can be seen in the lower panel of Figure ???. There is only weak emission detected in

1.5 Multi-configuration Image Cube Inspection

the same position in the corresponding C configuration channel maps, probably due to the lower sensitivity resulting from the smaller HPBW (i.e., the flux is diluted). This discrete second source thus has the effect of adding extra emission to the corresponding multi-configuration image cube spectrum at the low absolute velocities where it is present. The presence of this addition source at these low absolute velocities is probably one of the reasons why Huggins *et al.* (1994) did not detect a horned shaped spectrum with his 12'' HPBW. We also note that that there is a weaker emission feature 7'' north north-west of α Ori in these maps also which too can be seen in Figure ???. Finally, the Submillimeter Array CO($J = 3 - 2$) line profile will be discussed in Section 1.10 but here we confirm that its image cube also contains this spatially unresolved source $\sim 5''$ S-W of α Ori at the same velocities.

1.5 Multi-configuration Image Cube Inspection

A subset of the blueshifted velocity channel maps of the low spectral resolution multi-configuration image cube is presented in Figure ???. The first channel map at -17.9 km s^{-1} shows just the compact unresolved continuum emission with no extended emission present. Between -16.7 km s^{-1} and -9.0 km s^{-1} we see evidence for the development of a classical shell signature for the S2 flow. We first sample the highest velocity components where the emission is relatively compact (i.e. between -16.7 km s^{-1} and -12.9 km s^{-1}) and then sample lower absolute velocity components where S2 becomes a faint ring (i.e. between -11.6 km s^{-1} and -9.0 km s^{-1}). At lower velocities again, these rings disappear into the noise of the maps and possibly extend out beyond the primary beam at zero velocity where S2 should have maximum spatial extent. The emission from the channel maps between -15.3 km s^{-1} and -11.6 km s^{-1} correspond to all the emission in the extreme blue wing component of the multi-configuration image cube line profile discussed in Section 1.3. We can see in Figure ?? that all of this emission is greater than the C configuration resolving out scale of $\sim 6''$, therefore confirming that our C configuration line profile is mainly composed of S1 emission. The shell formation signature of S2 is also apparent in the redshifted velocity channel maps between $+7.5 \text{ km s}^{-1}$ and $+13.8 \text{ km s}^{-1}$ but the emission appears weaker and the

rings fainter confirming that S2 is inhomogeneous. The multi-configuration maps also show the central compact emission from the S1 flow at velocities between -10.3 km s^{-1} and $+11.3 \text{ km s}^{-1}$. This S1 emission can be seen in the final two maps of Figure ?? as a central slightly elongated emission feature surrounded by the fainter rings of the S2 flow.

1.6 Spatial Extent of S2

The spatial extent of the S2 flow around Betelgeuse was not directly determined from either the CO infrared absorption spectra of Bernat *et al.* (1979) or previous CO single dish radio observations (Huggins, 1987; Huggins *et al.*, 1994; Knapp *et al.*, 1980). Our low spectral resolution multi-configuration image cube has sufficient spatial resolution and S/N to make direct estimates of its maximum radius. We find that little or no signature of the S2 flow is present in the low absolute velocity channel maps where its spatial extent is maximum and either lies outside of the primary beam or is lost into the noise near the edge of the maps. Therefore we cannot make a simple direct measurement of its maximum size. However, by measuring how its size varies in the higher absolute velocity maps where it is clearly present allows us to derive its maximum spatial extent.

If we assume that S2 is spherically symmetric with an outer radius R_{S2} , and is undergoing steady expansion with velocity V_{S2} , then its geometry is described by Figure 1.6. As we sample the line at different velocities, the spatial extent of S2 changes and gets progressively larger at lower absolute velocities as can be seen in Figure ???. The projected radius of S2 in each map is

$$r_{\text{chan}} = R_{S2} \times \sin\theta \quad (1.3)$$

which can be directly measured in many of the channel maps. Each of these channel maps have an associated velocity V_{chan} , which we know, and is related to the actual velocity of the S2 flow by

$$V_{\text{chan}} = V_{S2} \times \cos\theta. \quad (1.4)$$

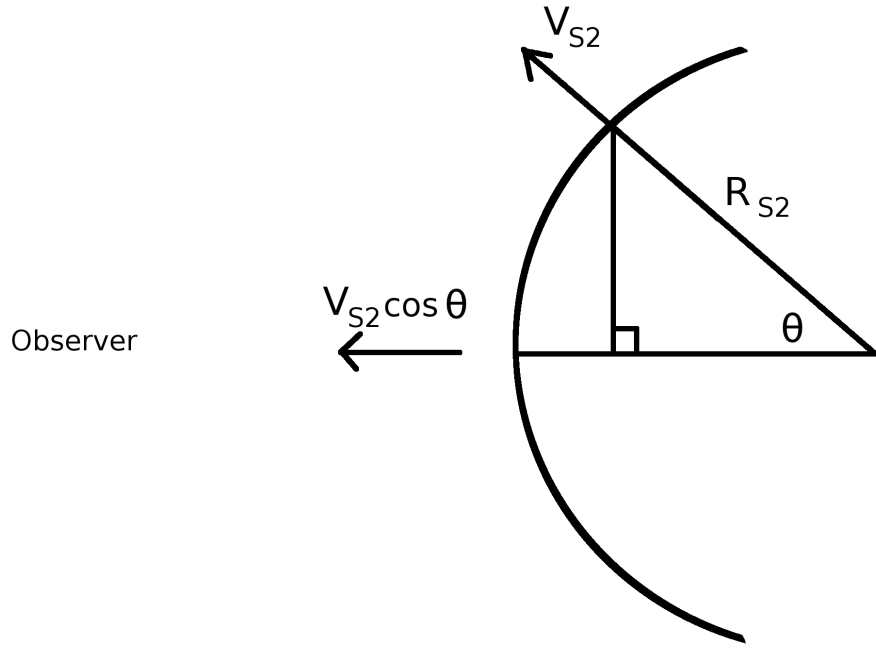


Figure 1.6: Geometry of a spherical symmetric flow used to derive the spatial extent of the S2 flow. By measuring the spatial extent of S2 (i.e., $R_{S2}\sin\theta$) as a function of channel/velocity (i.e., $V_{S2}\cos\theta$) the maximum spatial extent of the S2 flow can be derived.

Combining Equations 1.3 and 1.4 via the angle dependence, gives the following equation which contains R_{S2} as the only unknown parameter,

$$r_{\text{chan}} = R_{S2} \times \sin \left[\cos^{-1} \left(\frac{V_{\text{chan}}}{V_{S2}} \right) \right]. \quad (1.5)$$

An estimate of the S2 radius per channel (r_{chan}) was found by creating annuli of increasing radius around the central emission in each relevant line channel map of the multi-configuration image cube, extracting all flux within each annulus and then plotting the integrated flux against distance from the star for each channel map. The maximum of these resultant curves were then deemed to be the maximum radius of S2 per channel map. Figure 1.7 shows these data overplotted with two model outflows which were created using Equation 1.5. The blueshifted data points were best fitted by a model outflow having a maximum radius $17''$ and outflow velocity 16.7 km s^{-1} , while the redshifted data points were

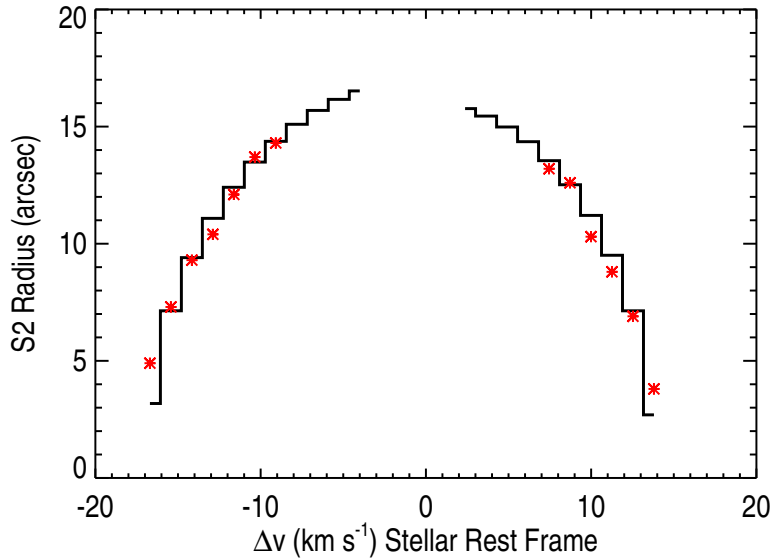


Figure 1.7: The derived S2 radius as a function of velocity (red points) overplotted with two model outflows. The blueshifted model (left) corresponds to an outflow with a maximum radius of $17''$ and a velocity of 16.7 km s^{-1} while the redshifted model (right) corresponds to an outflow with a maximum radius of $16''$ and a velocity of 13.8 km s^{-1} .

best fitted by a model outflow with a maximum radius $16''$ and outflow velocity 13.8 km s^{-1} . It is worth mentioning that this estimate for the spatial extent of S2 is only weakly dependent on our adopted radial velocity value for Betelgeuse and adopting a slightly different value would simply alter the outflow velocities.

1.7 Intensity distribution of CO

We first investigate how one would expect the intensity of CO to vary as a function of distance from the star for a spherically symmetric optically thin outflow. The CO($J = 2 - 1$) emission line is formed over an extended region around Betelgeuse so a constant outflow velocity can be assumed when investigating the intensity distribution of the S1 and S2 outflow. This allows us to use the equation of mass continuity to find the number density of the molecules in the lower level of the transition, n_l , i.e., $n_l \propto r^{-2}$. The Boltzmann formula can then be used to find

1.7 Intensity distribution of CO

the number density of CO molecules in the upper level, n_u ,

$$n_u(r) = n_l(r) \frac{g_u}{g_l} e^{-(E_u - E_l)/kT_{\text{exc}}(r)} \quad (1.6)$$

where g_u and g_l are the statistical weights of the two rotational levels, and E_u and E_l are their respective energies. Here, T_{exc} is the excitation temperature and equals to the gas temperature if collisions dominate the redistribution of the populations over the vibrational ladder. To find the intensity we first need to know the emissivity, j_l , of the line photons which is just $n_u(r)$ times the probability for spontaneous de-excitation per second, A_{ul} , times the energy of the emitted photons, $h\nu$, i.e.,

$$j_l(r) = n_u(r) A_{ul} h\nu \propto r^{-2} e^{-(E_u - E_l)/kT_{\text{exc}}(r)}. \quad (1.7)$$

If T_{exc} is constant, then the line intensity, I_{CO} , is the integral of the emissivity along the line of sight in direction z , at some impact parameter (or projected radius), R ,

$$I_{\text{CO}} = \int j_l(r) dz \propto R^{-1}. \quad (1.8)$$

Therefore, the intensity distribution for an optically thin spherically symmetric constant velocity outflow should vary as R^{-1} .

In the left column of Figure 1.8 we investigate the intensity distribution of CO emission as a function of projected radius, R , for both the S1 and S2 flows. From our discussions in Section 1.3 we can assume that all line emission between $-15.4 \rightarrow -10.3 \text{ km s}^{-1}$ and $+12.4 \rightarrow +13.8 \text{ km s}^{-1}$ emanates solely from the S2 flow. Using the low spectral resolution multi-configuration image cube we integrate the surface brightness over these channels and find that the intensity fall-off is close to being proportional to R^{-1} (Figure 1.8: *top left*). To investigate the S1 flow intensity distribution around α Ori we integrate the surface brightness over the channels between $-9 \rightarrow +10.6 \text{ km s}^{-1}$. Although these channels contain emission from both S1 and S2, most of the S2 emission here will have larger projected radii and thus the majority of the inner emission should emanate from the S1 flow. Between $0.5''$ and $4''$ from the star the intensity is again found to be close to proportional to R^{-1} (Figure 1.8: *bottom left*). We have just showed

1.7 Intensity distribution of CO

that such an intensity distribution is expected for an optically thin spherically symmetric constant velocity outflow with $\rho \propto 1/R^2$. Beyond $\sim 6''$ the intensity fall off is more rapid and is steeper than a R^{-2} distribution and may be caused by factors such as a variation in the thermal or velocity profile, or even the absence of emitting material altogether. This region may mark the initiation of the current epoch of mass-loss.

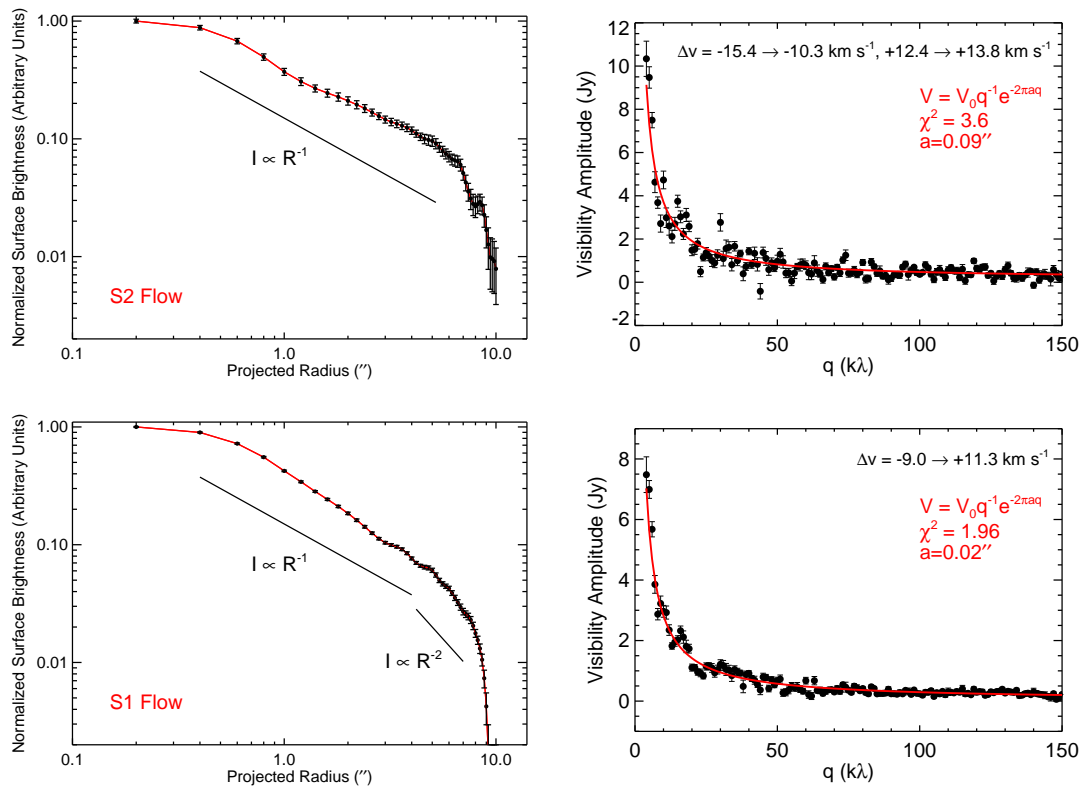


Figure 1.8: *Left Column:* Surface Brightness as a function of projected radius on sky, R (red line). The emission has been extracted from the low spectral resolution multi-configuration image cube and is integrated over the channels where S1 is present (bottom) and over the channels where only S2 is present (top). Intensity proportional to R^{-1} and R^{-2} is also shown for comparison. *Right Column:* The corresponding visibility amplitude as a function of $u-v$ distance (q) of both outflows can be modeled well by a R^{-1} fall off in intensity. The error bars in all plots represent the standard error of the mean.

Insight can also be gained into how the intensity varies on different size scales

by conducting analysis in the $u - v$ plane and plotting the visibility amplitude of our CO data against $u - v$ distance. The result of this is shown in the right column of Figure 1.8 where the same channels corresponding to the S1 and S2 flows defined in the last paragraph have been used. The data are azimuthally averaged, and have been binned to produce one data point per $k\lambda$. The result for both the S1 and S2 data is a steep drop-off in visibility amplitude over a relatively short $u - v$ distance, signaling that the sources are well resolved, as expected. Both sets of visibility data are consistent with an intensity proportional to $(a^2 + R^2)^{-1/2}$, where a is an inner spatial limit. This is because the Hankel transform of this function is $q^{-1}e^{-2\pi aq}$ (Bracewell, 2000), where q is the $u - v$ distance, and a vertically scaled version of this function is shown to match the visibility data very well in Figure 1.8. As analysis in both the sky and $u - v$ plane indicate the intensity of both flows is proportional to R^{-1} we conclude that both outflows are consistent with an optically thin and quasi-steady flow which is in agreement with Smith *et al.* (2009) (i.e., S1) and Plez & Lambert (2002) (i.e., S2).

1.8 Spatial Extent of S1

It is difficult to exactly determine of the maximum spatial extent of the S1 flow as we do not see the classical shell formation signature as we sample across velocities, like we do for the S2 flow. Its spatial extent varies in different channel maps and, as can be seen in Figure 1.9, the emission is very inhomogeneous/clumpy. This clumpy nature of the S1 flow has been previously reported in other studies (Kervella *et al.*, 2011; Smith *et al.*, 2009) and Smith *et al.* (2009), who studied photospheric scattered emission, estimated its spatial extent to lie within $3''$ from the star. At 20% of maximum emission in the integrated intensity S1 map (i.e. composed of all channels between $-9 \rightarrow +10.6 \text{ km s}^{-1}$) the S1 flow extends out to a mean distance of $\sim 4''$ and is even more extended in the S-W direction due to the presence of the second emission feature in the compact configuration data sets. Even though the emission is inhomogeneous, the intensity when averaged on the sky is consistent with a $\sim R^{-2}$ density distribution out to $\sim 6''$, as discussed in Section 1.7, and may mark the end of the S1 flow. The HPBW of $0.9''$ is

not sufficient to determine whether the S1 flow is discrete or an extension of the current wind phase seen in ultraviolet spectra (e.g., Carpenter & Robinson, 1997) and cm-radio continuum interferometry (Lim *et al.*, 1998).

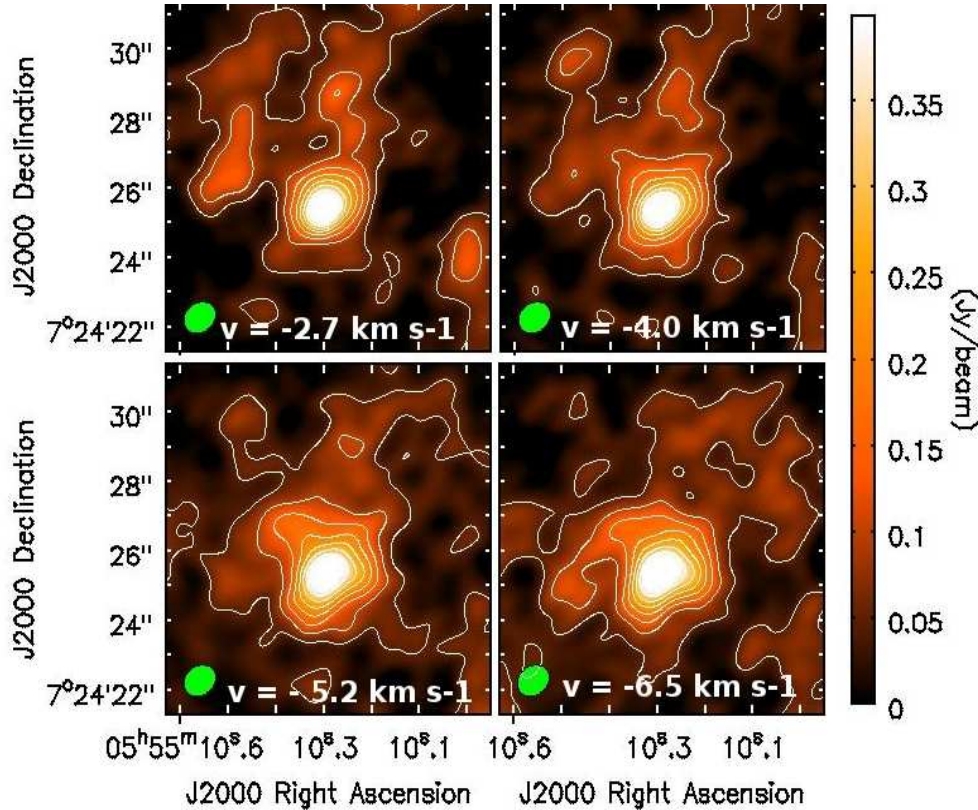


Figure 1.9: CARMA combined image cube low spectral resolution, 1.3 km s^{-1} , maps of the inner S1 flow. These maps are $10'' \times 10''$ in size and show the irregular nature of the S1 emission around the star. Going clockwise from the top left panel, the channel map velocities are -2.7 , -4.0 , -5.2 , and -6.5 km s^{-1} . The restoring beam is shown in green in the bottom left of each map. Contour levels are at $(3, 6, 9\dots) \times \sigma_{\text{rms}}$ where $\sigma_{\text{rms}} = 16 \text{ mJy beam}^{-1}$.

1.9 Continuum Flux Densities

Betelgeuse is known to show brightness variations at many continuum wavelengths. Goldberg (1984) reports a decrease of half a magnitude in visual brightness over a period of six years. Bookbinder *et al.* (1987) found stochastic 30%-40%

1.9 Continuum Flux Densities

variations in flux density at 6 cm over timescales as short as 10 days to as long as 8 months (i.e. the observational period). A more comprehensive study was carried out by Drake *et al.* (1992) who observed Betelgeuse with the VLA at centimeter wavelengths from 1986 to 1990 and found stochastic variability of 22%, 15%, and 21% at 6 cm, 3.6 cm, and 2 cm respectively, at a variety of different timescales down to less than one month (a possible source for this variability will be described in Section 1.11). The mm-continuum emission that we measure arises mainly from electron-ion and electron-atom bremsstrahlung (also the source of the longer wavelength continuum emission) and possibly dust emission, so it is not unreasonable to also expect variability at mm-wavelengths too.

Table 1.1: CARMA Continuum Fluxes at 230 GHz between 2007 → 2009.

Configuration	Date	Restoring Beam ("×")	Flux (mJy)	Uncertainty (mJy)
C	2007 Jun	0.96 × 0.76	234	18
D	2009 Jul	2.33 × 1.87	389	72
E	2009 Nov	4.93 × 3.84	278	40
Multi-configuration	2007 → 2009	1.05 × 0.84	289	21

In Table 1.1 we list the derived continuum flux densities for each of the three configuration image cubes and also the multi-configuration image cube. The high spectral resolution ($\Delta v = 0.65 \text{ km s}^{-1}$) image cubes were just wide enough to image the CO line but were too narrow to make accurate estimates of the continuum flux density. Therefore, all continuum flux density estimates are derived from the lower spectral resolution ($\Delta v = 1.3 \text{ km s}^{-1}$) image cubes from which we were able to take accurate measurements at both sides of the line. We fitted elliptical Gaussians to ~ 20 continuum channels using CASA’s *imfit* routine allowing the flux and corresponding uncertainties to be calculated. The source was unresolved in almost all of these continuum channels which means that the continuum emission is formed within $\sim 0.9''$. The D configuration data were acquired under adverse weather conditions and these data have the highest noise levels out of the three configurations. Its continuum emission measurement is approximately 50% greater than the C and E configuration continuum measurements which were also

1.10 Higher CO rotational lines

acquired approximately two years after the D configuration data. We believe the continuum emission value of 289 ± 21 mJy derived from the multi-configuration image cube is a reasonable estimation of the mean mm-continuum flux density over the 2.5 yr period, 2007 → 2009. It is in reasonably good agreement with the 250 GHz flux density of Altenhoff *et al.* (1994) who report a mean value of 351 ± 25 mJy for 1986 → 1989.

1.10 Higher CO rotational lines

As part of our larger multi-wavelength study of the CO surrounding Betelgeuse, we were also able to obtain emission line profiles of higher rotational CO lines. We observed the star (PI Harper: ID 81-0005-1) with the German Receiver for Astronomy at Terahertz Frequencies (GREAT; Guesten *et al.*, 2000) instrument on NASA and DLR's Stratospheric Observatory for Infrared Astronomy (SOFIA; Becklin & Gehrzi, 2009) 2.5 m airborne observatory. Observations of the CO($J = 12 - 11$; 1.382 THz) line were made during Flight 86 on 2011 November 10 at 13,100 m ($\sim 43,000$ ft) when the star had an elevation of 45° . The HPBW was $\sim 19''$ and the effective on source exposure time was 12 minutes, which was considerably lower than the requested on source time of 70 minutes due to technical difficulties during the flight. We also obtained 4.1 hours on source at 345 GHz with the Submillimeter Array (SMA; Blundell, 2007) on 2012 January 12 (PI J. Brown: ID 2011B-S051). The SMA is a submillimeter interferometer located atop Mauna Kea in Hawaii and consists of eight antennas, each 6 m in diameter. Our data were acquired in the compact configuration ($B_{\max} = 70$ m) which at the observing frequency of ~ 345 GHz, gave a synthesized beam of 5×4.5 arcsec 2 (similar to the CARMA E configuration at 230 GHz). We obtained very high spectral resolution ($\Delta v = 0.088$ km s $^{-1}$) of the CO($J = 3 - 2$; 345.796 GHz) line which is more than a factor of 7 better than the highest spectral resolution CARMA data. Finally we obtained archival data of the CO($J = 6 - 5$; 691.473 GHz), CO($J = 10 - 9$; 1.15198 THz), and CO($J = 16 - 15$; 1.84135 THz) rotational lines which were obtained with the Heterodyne Instrument for the Far Infrared (HIFI; de Graauw *et al.*, 2010), on board the Herschel Space Observatory

1.10 Higher CO rotational lines

(Pilbratt *et al.*, 2010). The HPBW for these lines were $31''$, $18''$, and $11.5''$, for the $J = 6 - 5$, $J = 10 - 9$, and $J = 16 - 15$ transitions, respectively.

We plot all these line profiles in order of excitation energy in the stellar rest frame in Figure 1.10, to allow easy comparison. The profiles have been binned to 1.3 km s^{-1} spectral resolution to match the CARMA low resolution profiles described in Section 1.3, except for the SMA profile which has excellent spectral resolution. In this figure the dashed vertical red lines mark the derived outflow velocities of the S1 flow from Section 1.3. This figure clearly demonstrates that the CO rotational lines get narrower as one goes from lower rotational levels to higher ones, i.e., as the excitation temperature increases. A noticeable consequence of this is the evolution of the contribution of the S2 blueshifted component which is the dominant feature in the $\text{CO}(J = 2 - 1)$ combined configuration CARMA profile; its relative strength in relation to the rest of the line dramatically reduces at higher excitation temperatures. This indicates that the higher lines are predominately formed in the S1 flow region. The SOFIA $\text{CO}(J = 12 - 11)$ profile is found to have a line width of $\sim \pm 7.5 \text{ km s}^{-1}$ when centered on the stellar rest frame but because the higher S/N $\text{CO}(J = 16 - 15)$ HIFI profile is slightly wider, the narrowness of the SOFIA line is probably due to its low S/N.

For the lower rotational line profiles, it is difficult to infer the level of flux contribution from each of the S1 and S2 components making the analysis of integrated line flux ratios difficult. Also, some of these profiles shown in Figure 1.10 were obtained over many years with different instruments and techniques. It appears likely however, that the majority of the emission in the higher rotational profiles [i.e., the $\text{CO}(J = 16 - 15)$, $\text{CO}(J = 12 - 11)$, and $\text{CO}(J = 10 - 9)$ line profiles] emanates from the S1 flow, while the other lower level lines contain various amounts of emission from both flows. However, the $\text{CO}(J = 12 - 11)$ line profile has a low S/N and its flux scale is rather uncertain due to the poor pointing accuracy during our SOFIA-GREAT observation. For this reason only the Herschel/HIFI $\text{CO}(J = 16 - 15)$ and the $\text{CO}(J = 10 - 9)$ line profiles are suited for probing the thermodynamics of one of the flows, i.e., the S1 flow.

The ratio of the integrated flux from these two rotational emission lines in a

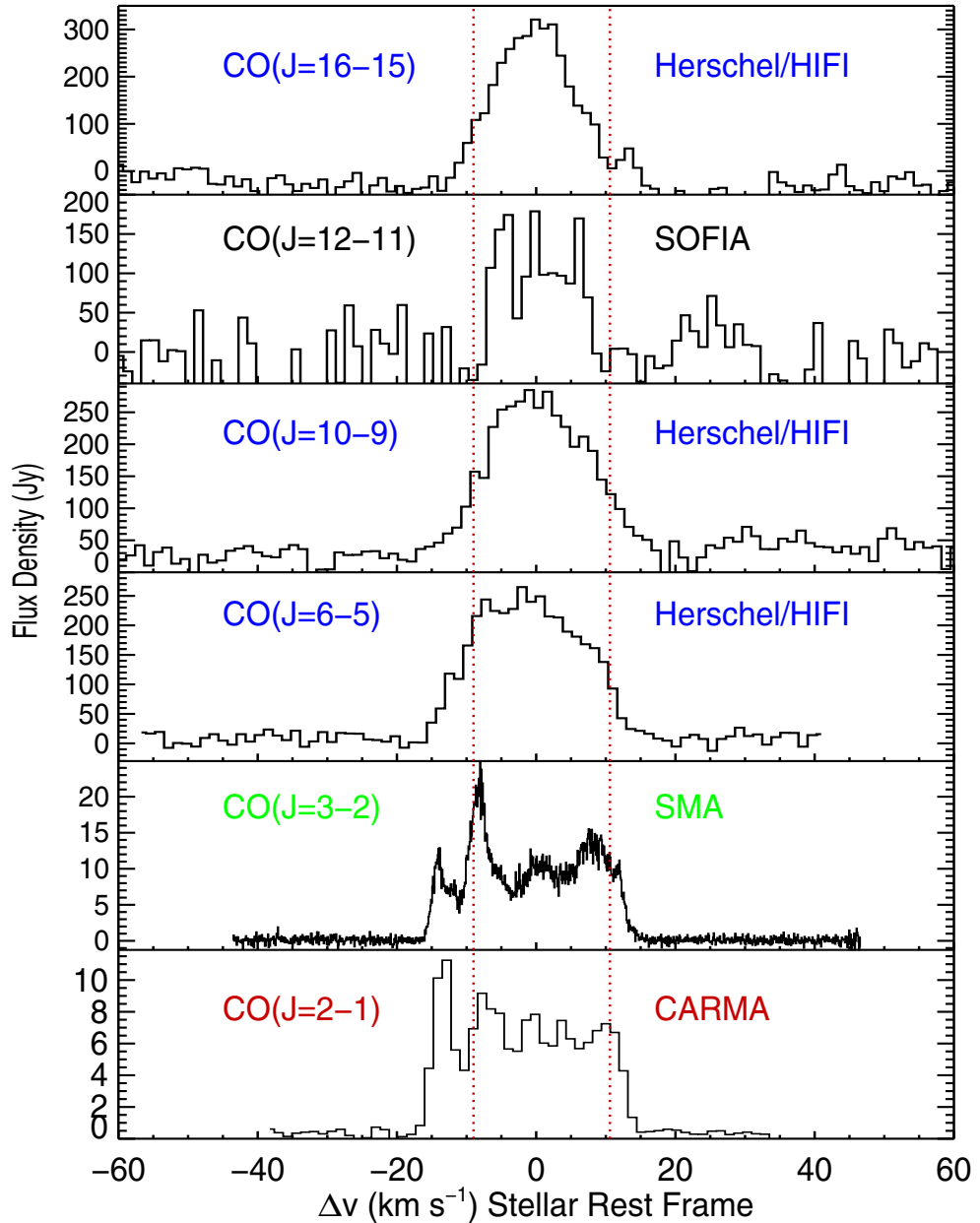


Figure 1.10: CO rotational emission lines from the CSE of Betelgeuse. The lines are listed in order of decreasing excitation energy from top to bottom, and are plotted in the stellar rest frame. The vertical dashed red lines mark the outflow velocities of the S1 flow. At higher excitation energies the relative strength of the blueshifted S2 feature in relation to the rest of the line decreases dramatically and the lines get narrower. This indicates that the higher excitation lines are formed mainly in the S1 flow.

1.10 Higher CO rotational lines

linear molecule like CO can be written as

$$\frac{F_{10-9}}{F_{16-15}} = \left(\frac{J_{10}}{J_{16}} \right)^5 \exp \left(\frac{B_v [J_{16}(J_{16}+1) - J_{10}(J_{10}+1)]}{T_{\text{exc}}} \right) \quad (1.9)$$

where F , J , and B_v are the integrated line flux, the rotational quantum number, and the rotational constant, respectively. For the CO molecule, $B_v = 2.77 \text{ K}$. Equation 1.9 is derived from the relation, $F_{j,j-1} \propto n_j A_{j,j-1} h\nu_{j,j-1}$, where n_j and $A_{j,j-1}$ are found from Equations ?? and ???. The integrated line fluxes for the CO($J = 16 - 15$) and the CO($J = 10 - 9$) profiles are 2.4×10^{-16} and $1.8 \times 10^{-16} \text{ W m}^2$, respectively. Equation 1.9 can then be used to show $T_{\text{exc}} = 220 \text{ K}$. This is in excellent agreement with Bernat *et al.*'s 1979 value of $200^{+50}_{-10} \text{ K}$ for the S1 flow who analyzed ro-vibrational fundamental lines near $4.6 \mu\text{m}$.

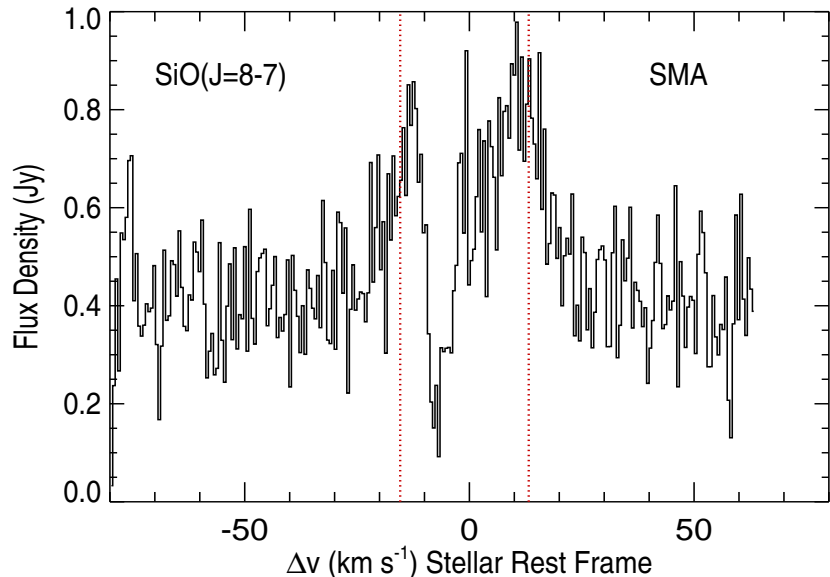


Figure 1.11: SiO($J = 8 - 7$) rotational emission line from the CSE of Betelgeuse obtained using the SMA. The linewidth is similar to the CARMA combined configuration CO($J = 2 - 1$) line profile, signaling that the S2 flow contains SiO. The dotted red lines are the previously derived S2 outflow velocities.

Through a judicious choice of the SMA correlator setup, we simultaneously observed the SiO($J = 8 - 7$; 347.331 GHz) line while observing the CO($J = 3 - 2$) line. We report a weak detection of SiO($J = 8 - 7$) at a spectral resolution of 0.55 km s^{-1} , as shown in Figure 1.11. Previous searches for SiO in the CSE of

Betelgeuse have been unsuccessful (e.g., Lambert & Vanden Bout, 1978) and this may be the first, albeit weak, detection of the molecule. The weak SiO($J = 8 - 7$) line profile is unfortunately contaminated with an atmospheric absorption feature but its linewidth is comparable to the CO($J = 2 - 1$) line profile, which means that SiO is also present in the S2 flow. A crude estimate of the CO($J = 8 - 7$) flux density from the S2 flow can be found by taking the mean value of the blueshifted emission feature in the Herschel $J = 10 - 9$ and $J = 6 - 5$ lines. From this we see that CO is ~ 100 times more abundant in the S2 flow than SiO. For an O-rich star like Betelgeuse we can expect that all C and Si will be in the form of CO and SiO, respectively. The CO/SiO ratio should then represent the C/Si ratio. Assuming solar abundances¹ this ratio should be only ~ 8 . The much larger ratio observed is probably a consequence of the role played by SiO molecules in the formation of silicate dust.

1.11 CARMA CO observations in Context

We have found the spatial extent of the S2 flow to be greater than the HPBWs of some of the previous single dish antenna observations of the CO($J = 2 - 1$) line. So why did these single dish line profiles not show the classical resolved signature of high emission at large absolute velocities and low emission at low absolute velocities? First, the S1 flow was still unresolved in these single dish observations and thus contributes emission at the lower absolute velocities. As well as this, the multi-configuration CARMA maps show that the S2 emission is brighter at higher absolute velocities than at lower absolute velocities and so when the emission from the fainter rings is neglected (i.e., when observed with a small HPBW), the overall line profile does not change significantly. Finally, our maps have revealed that some discrete strong emission features are present at low absolute velocities, which would also have been present in the HPBW of previous single dish observations, thus contributing to the line profile flux at these velocities.

The main properties of the S1 and S2 flows, which have been derived in the previous sections of this chapter, are summarized in Table 1.2. Assuming a mean

¹As Betelgeuse is a Population I star

1.11 CARMA CO observations in Context

outflow velocity of 14.3 km s^{-1} and 9.8 km s^{-1} for the S2 and S1 flows respectively, then their ages are ~ 1100 yr and $\sim 400 - 600$ yr. Since Plez & Lambert (2002) have detected K I out to $55''$ at a similar velocity (i.e., $18 \pm 2 \text{ km s}^{-1}$) to the CO S2 flow, then, assuming the CO and K I are coupled, there appears to be little further acceleration in Betelgeuse's outflow once the S2 flow begins (which is somewhere greater than $6''$).

Table 1.2: Summary of the S1 and S2 Flow Properties.

	S1	S2
Outflow Velocities (km s^{-1})	$-9.0 \& +10.6$	$-15.4 \& +13.2$
Maximum Spatial Extent ('')	$\sim 4 \rightarrow 6$	~ 17
Age (yr)	$\sim 400 \rightarrow 600$	1100

Despite decades of research, it is unknown if Betelgeuse loses mass through episodic ejections or through more of a constant and global process. We have shown that when averaged across the sky, the variation in mean density is consistent with a spherically symmetric and constant velocity outflow. However, the presence of clumping is also evident in our radio maps and emission from the S2 flow appears weaker at redshifted stellar rest frame velocities indicating an inhomogeneous flow. Higher spatial resolution studies like those described in the following sections, are needed to determine if clumping is a result of growing instabilities in a global outflow or as a product of the mass-loss mechanism. The reason for two unique velocities in the outflow are also a puzzle. One possibility is that the dust properties change at $\sim 6''$ leading to a sudden acceleration of the flow. However, the S2 component has a small velocity dispersion along the line of sight (Bernat *et al.*, 1979) and appears as a shell like structure in our CARMA data so this scenario is unlikely. Another possibility is that the mass-loss mechanism is magnetic in origin and that these components represent phases in the order of ~ 600 yr of a stellar dynamo cycle (Harper, 2013).

1.12 e-Merlin 6 cm Results

The first detailed study of Betelgeuse at centimeter wavelengths was carried out by Newell & Hjellming (1982) who observed the star at multiple wavelengths (20, 6, 2, and 1.3 cm) in a compact VLA configuration. The star was unresolved but a radio spectral index of 1.32 was derived and the radio emission was interpreted as emanating from a spherically symmetric, partially ionized chromosphere with an temperature of $\sim 10,000$ K extending from 1 to $4 R_\star$, in agreement with the Alfvén wave models of the time (Hartmann & Avrett, 1984). The star was first spatially resolved at radio wavelengths by Skinner *et al.* (1997) with both the “old” VLA in its most extended configuration, and MERLIN (the predecessor to e-MERLIN). The data were taken ~ 2.5 yr apart and it was found that the 6 cm radio emitting region was up to three times larger than the optical photosphere. The spatially resolved multi-wavelength study of Lim *et al.* (1998) revealed a cool, low hydrogen ionization inner atmosphere. To reconcile these observations with spatially resolved UV observations Gilliland & Dupree (1996), which showed a much warmer inner atmosphere, Lim *et al.* (1998) concluded that there must be at least 3 orders of magnitude more cooler plasma than hot chromospheric plasma. This is because the radio opacity of the warm more ionized gas is much greater than that of the cooler less ionized gas, and yet the radio observations of Lim *et al.* (1998) preferentially detect the cooler gas. We now discuss the recent findings of Richards *et al.* (2013) who observed Betelgeuse at 6 cm with the very long baseline interferometer, e-MERLIN.

e-MERLIN (Muxlow, 2003) consists of seven radio antennas spread out across the United Kingdom that are connected via a fiber optic network to a central correlator at Jodrell Bank Observatory. It will eventually be able to observe in three frequency bands at 1.3 – 1.8 GHz, 4 – 8 GHz, 22 – 24 GHz, and its maximum baseline of 220 km will provide resolution up to 10 mas at the μ Jy sensitivity level. Betelgeuse was observed at 5.76 GHz (5.2 cm) in 2012 July with e-MERLIN as part of Cycle-0 observations, with a total bandwidth of 0.512 GHz. The final high resolution image which is shown in Figure 1.12 had a $\sigma_{\text{rms}} = 9 \mu\text{Jy}$ and was produced using uniform weighting with a restoring beam of 80×60 mas 2 . The first thing to notice about the radio map is the presence of three clumps of radio

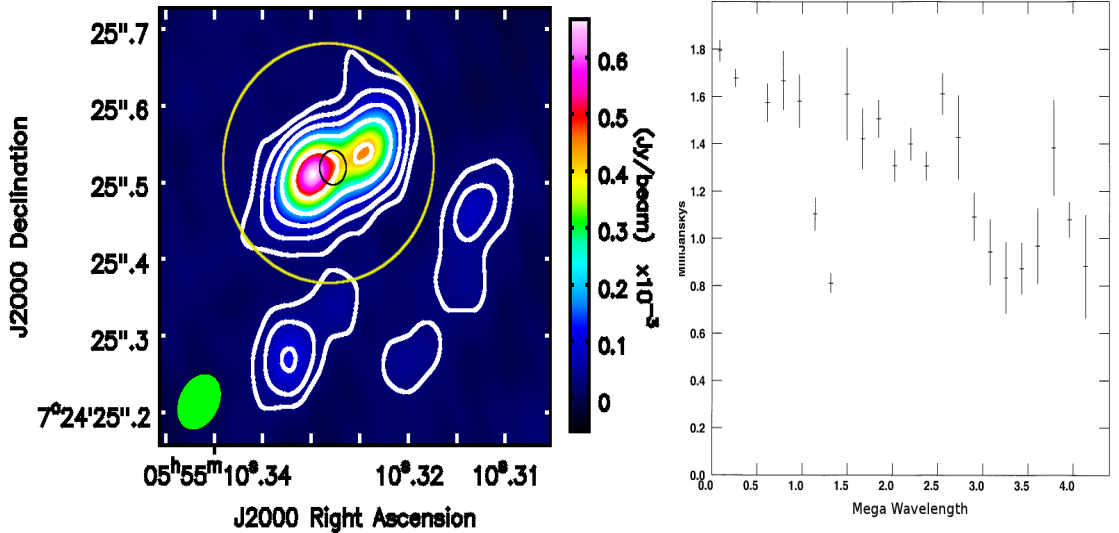


Figure 1.12: First e-MERLIN results for Betelgeuse. *Left:* 5.2 cm e-MERLIN image of Betelgeuse taken in July 2012 showing two unresolved emission features separated by 90 ± 10 mas. The image was restored with a 80×60 mas 2 beam marked in green in the lower left corner and using uniform weighting. Contour levels are at $(-3, 3, 6, 12, 24, 48) \times \sigma_{\text{rms}}$ where $\sigma_{\text{rms}} = 9 \mu\text{Jy}$. The photospheric radius is the small black circle while the large yellow circle defines the 6 cm radio disk of Lim *et al.* (1998). *Right:* The calibrated visibility amplitudes (in mJy) versus $u - v$ distance measured in mega-wavelengths with the possible signature of two unresolved components with a brightness ratio differing from unity.

emission in the south-west quadrant approximately 250 mas ($11.5 R_\star$) from the star, with detections ranging from 4 to $12\sigma_{\text{rms}}$. These clumps of radio emitting plasma may be the remnants of past localized episodic mass-loss events from the star, which as they escaped the gravitational potential of the star, expanded, cooled allowing hydrogen to recombine and thus in the process becoming fainter radio continuum emitters than they initially were. Assuming a mean constant flow velocity of 10 km s^{-1} (the velocity of the S1 flow), then this plasma was ejected from the star ~ 22 yr prior to these observations. The time since ejection could in fact be much larger than this (~ 90 yr) if the slow wind acceleration profile given in Harper *et al.* (2001) is assumed.

1.12 e-Merlin 6 cm Results

The second and more remarkable feature of the image is that the star at 6 cm appears as two unresolved peaks separated by ~ 90 mas. To make sure this unexpected result was not an artifact of the imaging process we plotted the visibility amplitude as a function of baseline (i.e., $\sqrt{u^2 + v^2}$) as shown also in Figure 1.12. If we had fully resolved a standard uniform disk, which should be a good first order approximation for any *standard* star, then we would expect the visibility amplitude to drop to zero at some baseline, which clearly does not happen. On the other hand, the visibility amplitude for a double source would depict two peaks with the minimum visibility amplitude being a function of the component brightness ratio. For equal brightness (i.e., the ratio is 1) the first visibility amplitude minimum drops to zero but does not for sources of different brightness (Saha, 2011). Therefore, the visibility amplitudes of our calibrated data appear to be in agreement with what is seen in the final image, i.e., two sources of different brightness producing a sinusoidal visibility pattern which does not drop to zero.

The brighter feature was found to have a brightness temperature of $T_b = 5,400 \pm 600$ K while the weaker feature had $T_b = 3,800 \pm 500$ K. To find the position of the optical photosphere, Richards *et al.* (2013) took the peak flux position from a low resolution radio map which was optimized for sensitivity to extended structure. In this scenario the two features, referred to as *hotspots* by Richards *et al.* (2013) are located $\sim 1.0 R_\star$ ($T_b = 5,400$ K) and $\sim 1.5 R_\star$ ($T_b = 3,800$ K) from the optical photosphere. A more rigorous approach to finding the position of the optical photosphere is to use the astrometric solutions derived in a study to find the distance to Betelgeuse (solution 5 in Harper *et al.*, 2008) and propagate these forward to find its expected position in 2012 July. Doing this we get RA = 05:55:10.3250 and Dec = +07:24:25.536 which includes the correction for parallax. We plot this expected position on top of the e-MERLIN map in Figure 1.13. Interestingly, this puts the expected optical photospheric position almost directly on top of the weaker emission feature. The effective temperature of Betelgeuse is 3,650 K (Levesque *et al.*, 2005) which is slightly below the brightness temperature derived for this feature but well within its errors (i.e., $T_b = 3,800 \pm 500$ K). If this weaker source is indeed the optical photosphere, then the brighter source with $T_b = 5,400 \pm 600$ K is located at least

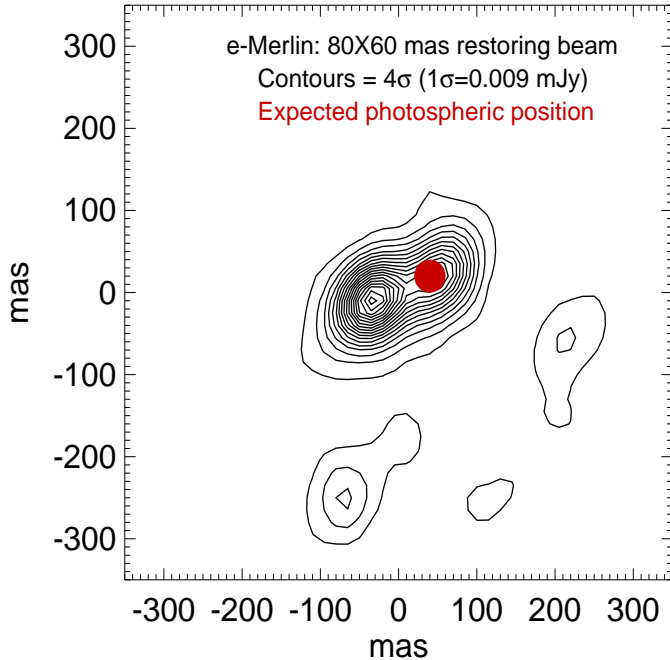


Figure 1.13: The red filled circle marks the predicted position of the optical photosphere of Betelgeuse on 2012 July using the astrometric solutions of Harper *et al.* (2001). The black contours represent the high spatial resolution 6 cm image of the star from Richards *et al.* (2013) and are at the $4\sigma_{\text{rms}}$ level. This solution puts the optical photospheric position almost at the position of the weaker unresolved peak.

$3.5 R_\star$ from the surface of the optical photosphere. Its value is significantly higher than that predicted in the spherically symmetric semi-empirical model of Harper *et al.* (2001) who predict a value of 2,300 K at a projected radius of 95 mas (i.e., $3.5 R_\star$ from the photosphere).

The semi-empirical model of Harper *et al.* (2001) is the current *state of the art* inner (i.e., $1 \rightarrow 10 R_\star$) atmospheric model for Betelgeuse. It consists of a detailed mean density and temperature 1-D model and is based on the spatially resolved VLA data of Lim *et al.* (1998). In this model the temperature distribution peaks at $1.45 R_\star$ where it reaches ~ 3800 K and decreases to ~ 1200 K at $10 R_\star$. The dominant source of electrons is from photoionized metals while hydrogen has a low level of ionization. We use this model to create a two-dimensional spherically

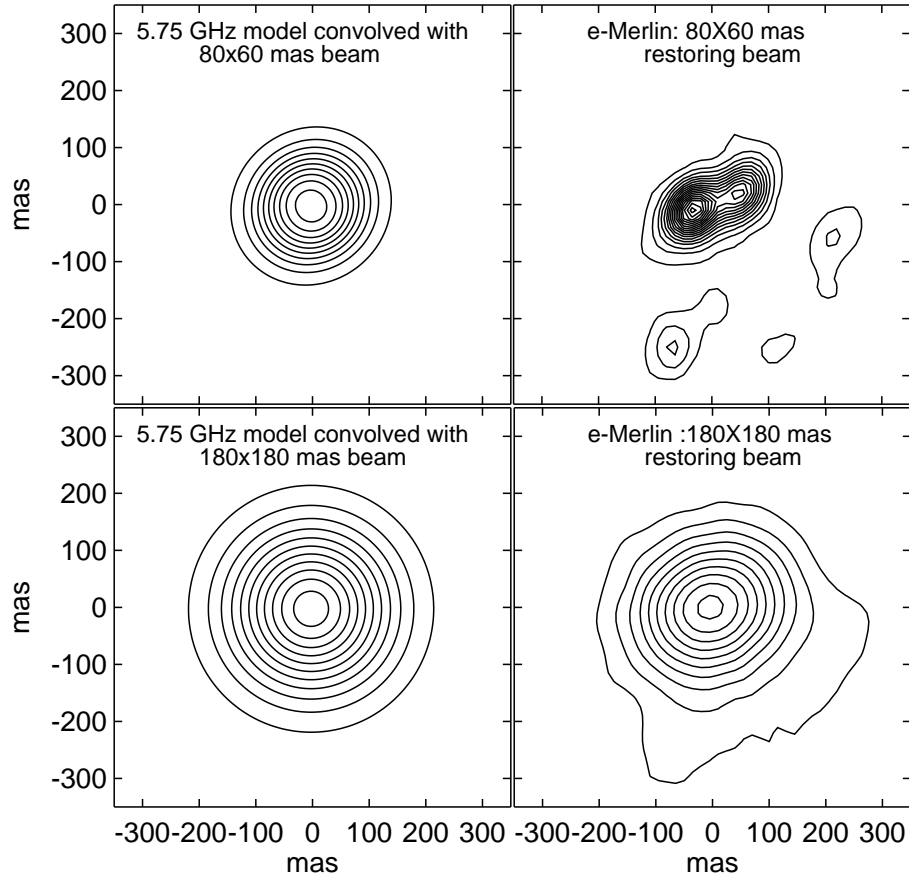


Figure 1.14: *Left column:* Two-dimensional specific intensity contour maps at 5.2 cm (5.75 GHz) created using the 1-D inner atmospheric model of Betelgeuse by Harper *et al.* (2001). The maps have been convolved with a beam having dimensions $80 \times 60 \text{ mas}^2$ (top) and $180 \times 180 \text{ mas}^2$ (bottom). *Right column:* The observed high (top) and low (bottom) resolution e-MERLIN images. The high resolution image is poorly described by the model of Harper *et al.* (2001) highlighting the inadequacies of 1-D spherically symmetric models in describing the inner atmosphere of Betelgeuse. Contour levels are $(4, 8, 12, \dots) \times \sigma_{\text{rms}}$ where $\sigma_{\text{rms}} = 6 \mu \text{Jy}$ in the top row and $\sigma_{\text{rms}} = 27 \mu \text{Jy}$ in the bottom row.

symmetric specific intensity map to examine how it compares with the new e-MERLIN high resolution data at 5.2 cm (5.75 GHz). As shown in Figure 1.14, we convolved this map with a restoring beam, first with dimensions $180 \times 180 \text{ mas}^2$ to match the low resolution e-MERLIN image and then with dimensions $80 \times 60 \text{ mas}^2$ to match the high resolution e-MERLIN image. As can be seen from

Figure 1.14, the atmospheric model of Harper *et al.* (2001) does a good job in reproducing the low resolution e-MERLIN image but, as would be expected from a spherically symmetric 1-D model, fails to reproduce the more complex structure which is seen in the higher resolution e-MERLIN image. The advent of the new e-MERLIN interferometer with its superior spatial resolution to that of the VLA has revealed that 1-D spherically symmetric atmospheric models are probably inadequate to describe the inner wind conditions of Betelgeuse. Time dependent models which radically diverge from spherical symmetry will ultimately be needed to accurately describe the inner atmospheric conditions of Betelgeuse.

1.13 VLA-Pie Town Maps vs e-MERLIN

At the end of Chapter ?? the VLA-Pie Town observations of Betelgeuse from the early 2000's were described, along with the motivation for analyzing it. In summary, we wanted to see if there were some signatures of the e-MERLIN asymmetries in the data set. This is because the Pie-Town link, when connected to the VLA, provides spatial resolution comparable to or exceeding that of the high resolution e-MERLIN image at the shortest wavelengths. The two main features present in the e-MERLIN map were separated by ~ 90 mas and so the most interesting VLA-Pie Town data sets were the 0.7, 1.3, and 2.0 cm maps which had restoring beams of $\sim 40 \times 25$, $\sim 80 \times 40$, and $\sim 120 \times 90$ mas² when imaged with uniform weighting.

All the data sets listed in Table ?? were CLEANed using uniform weighting and using a conservative, slow CLEAN to accommodate the frequent elliptical shape of the beam caused by the Pie Town link. The images were subsequently investigated for signs of asymmetries. The 6 cm VLA-Pie Town data sets had synthesized beams typically of size $\sim 380 \times 270$ mas² and were too large to be capable of resolving the structures seen with e-MERLIN at similar wavelengths. As expected, the VLA-Pie Town 6 cm images show no signs of asymmetries. In fact, all data sets at wavelengths at or longer than 1.3 cm show no obvious asymmetries apart from that caused by the asymmetric nature of the restoring beam. This is surprising because the north-west location of the Pie Town antenna relative to the VLA array results in an elliptical beam with a semi-minor axis

1.13 VLA-Pie Town Maps vs e-MERLIN

lying in the same direction as that of the two peaks seen with e-MERLIN, i.e., the beam shape should be well suited to resolving these peaks. There are two possible reasons why the shorter wavelength VLA-Pie Town maps do not contain the asymmetries which are present in the longer wavelength e-MERLIN map:

1. In an ionized or partially ionized outflow, the radio opacity, $\kappa_\lambda \propto \lambda^{2.1}$. This means that the longer wavelengths probe farther out in the atmosphere than the shorter wavelengths. It is possible that at the short wavelengths (where the VLA-Pie Town data have the capability to resolve these features) the outer atmosphere where the features are located is optically thin (i.e., $\tau_\lambda \ll 1$), and therefore the features are not present in the short wavelength VLA-Pie Town maps. However, the e-MERLIN data have shown that the outflow is clearly not spherically symmetric. In fact, the radio opacity also varies as, $\kappa_\lambda \propto n_e n_{\text{ion}}$, and because the e-MERLIN features should be more ionized than the surround plasma, they could be present even at the shortest wavelengths.
2. The VLA-Pie Town data were taken ~ 10 yr prior to the e-MERLIN data when the separation of the two peaks may have been less. This reduction in separation could be so significant that they could be unresolvable even at the shortest wavelengths. Let us now consider this possibility and estimate their separation 10 yr prior to the e-MERLIN observations. First, as highlighted in the Section 1.12, the astrometric solutions of Harper *et al.* (2008) indicate that the star is located on the weaker emission peak. If we then assume that the stronger emission peak has been moving away from the star at the velocity of the S1 flow (i.e, 10 km s^{-1}) then the distance traversed in 10 yr would be $\sim 4.8 R_\star$ which means that these features would not have been resolvable. However, the outflow is still expected to be accelerating with velocities only between $1 - 7 \text{ km s}^{-1}$ within these spatial scales (Carpenter & Robinson, 1997) and so the actual distance traversed is probably much less than $4.8 R_\star$.

At these spatial scales the structural changes over a few years will probably be important and may be the reason for not seeing the expected asymmetries

1.14 Long Term Radio Variability and Thermal Structure

in the VLA-Pie Town data. In fact, if the star is close to the center of these two peaks as was assumed by Richards *et al.* (2013), then the two features are presumably moving away from each other which would strengthen the idea that time variability is the reason why they are not seen in the VLA-Pie Town data. The discovery of these bright radio peaks by Richards *et al.* (2013) along with their notable absence in data with superior resolution less than 10 yrs before (albeit at higher frequencies) is a compelling case for consistent monitoring with e-MERLIN over a number of years at multiple wavelengths.

1.14 Long Term Radio Variability and Thermal Structure

Betelgeuse’s atmosphere is optically thick at radio wavelengths allowing its radio flux to be characterized as resulting from an opaque disk with $F_\nu \propto T_e \phi_\nu^2$. This relationship tells us that variations in radio flux are caused by changes in size or changes in the gas temperature distribution. The size of the radio emitting region is controlled mainly by the distribution in ionized material. Betelgeuse has been observed at radio wavelengths since the mid 1970’s (e.g. Newell & Hjellming, 1982). Bookbinder *et al.* (1987) found that the 6 cm flux can vary by as much as $\sim 40\%$ over a 20 day timescale, while Drake *et al.* (1992) monitored the star over a four year period and reported stochastic flux variability at 2.0 and 3.6 cm of $\lesssim 25\%$ and possibly at 6 cm on a timescale $\lesssim 1$ month. Here we report on how the radio flux has varied during the period 1996 – 2004 using the measurements of Lim *et al.* (1998) and the archival VLA-Pie Town data.

To obtain a value for the total flux density at each wavelength and epoch, we fitted 2-D Gaussians to the source to obtain the integrated flux. To get a better fit to the 0.7 cm data, (where the source size was found to be asymmetric as outlined in the next section) we re-imaged the visibilities using natural weighting and then carried out the fit. We plot the resulting flux densities against time in Figure 1.15 and also include the measurements of Lim *et al.* (1998). We find significant variability at all wavelengths and at all epochs apart from the 2002 data sets which were only obtained two months apart from each other. Over the 10 yr period, the maximum variability is found to be 23, 27, 32, 21, and 35% at

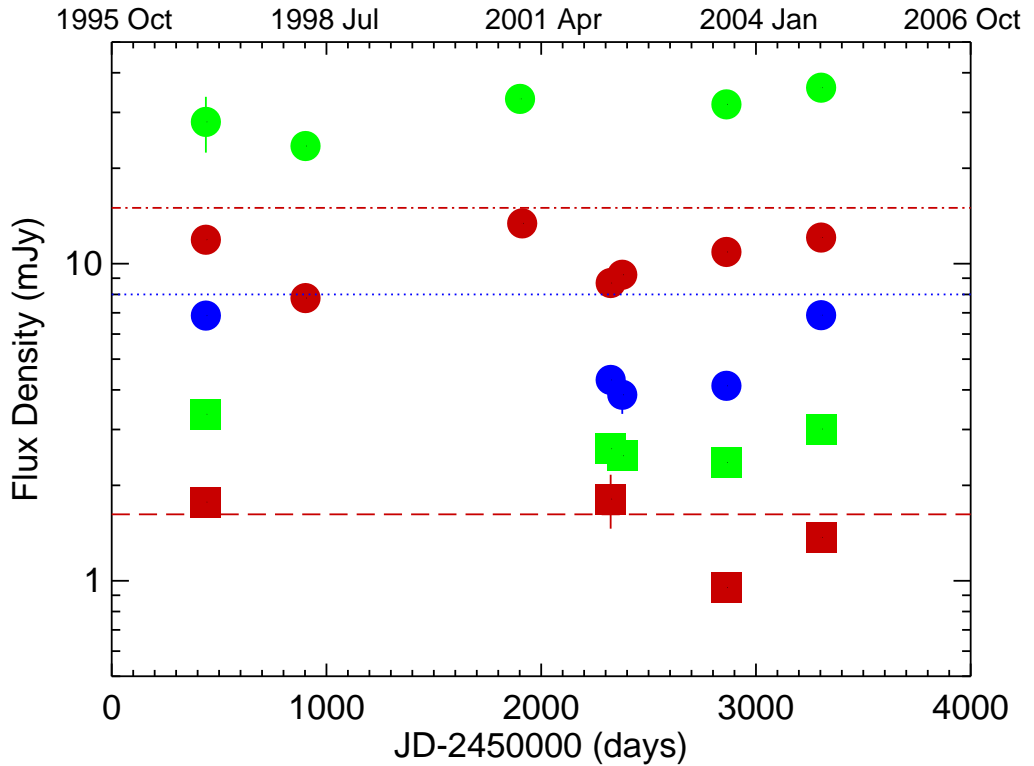


Figure 1.15: Radio flux density variation of Betelgeuse between 1996 and 2004. The green, red, and blue filled circles are the 0.7, 1.3, and 2.0 cm measurements respectively, while the green and red filled squares are the 3.5 and 6.2 measurements, respectively. The red dot-dash line and the blue dotted line represent the mean of two 1.3 and 2.0 cm flux density values taken between 1978-1981 and are not significantly different from the data plotted. The dashed red line represents the e-MERLIN 6 cm flux from 2012 and lies within the range of 6 cm values observed between 1996 and 2004.

0.7, 1.3, 2.0, 3.5, and 6.2 cm respectively, which are similar to those reported by Drake *et al.* (1992) and Bookbinder *et al.* (1987). The shortest wavelengths (i.e., 0.7 and 1.3 cm) are the most sampled and although there are only five data points at these wavelengths to compare, there does appear to be a correlation in their flux variability. The contribution functions given in Harper *et al.* (2001) show that the peak flux contribution at both 0.7 and 1.3 cm come from a similar region of the atmosphere (i.e., $\sim 1.2 R_*$) and so at these wavelengths a correlation is not surprising.

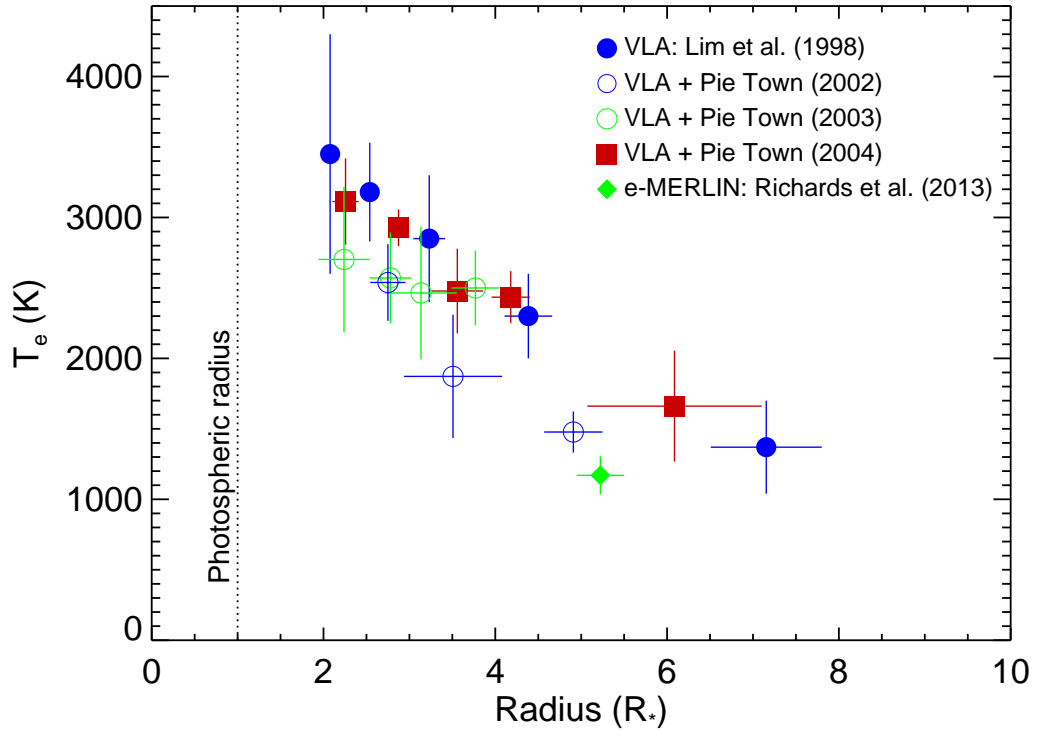


Figure 1.16: Mean thermal profile of Betelgeuse’s inner atmosphere using spatially resolved radio data spanning 1998–2013. Our VLA + Pie Town data confirm the relatively low temperature (< 4000 K) of Betelgeuse’s expended atmosphere. Uniform bright disks were fitted to the calibrated visibilities at each wavelength allowing the temperature to be derived as a function of distance from the star.

The red dot-dash line and the blue dotted line in Figure 1.15 represent the mean of the two 1.3 and 2.0 cm flux density values between 1978 – 1981 (Newell & Hjellming, 1982) which are not significantly different from our maximum measurements at the same wavelengths. This would indicate that there has been no significant long term change in atmospheric or thermal structure over ~ 3 decades. However, the flux variability may be a manifestation of significant structural changes or thermal changes over the order of only a few years. The dashed red line represents the 6 cm flux of Richards *et al.* (2013) which lies within the range of 6 cm values observed between 1996 and 2004. This is surprising because most of the 6 cm flux in the e-MERLIN map is contained in the two bright fea-

tures and as we see no evidence for these features in our VLA-Pie Town data, we would expect the 6 cm flux in the e-MERLIN map to be larger. This adds weight to the idea discussed in Section 1.13 that the e-MERLIN feature(s) are optically thin at the shorter VLA wavelengths and therefore are not detectable in our highest resolution data sets. Nevertheless, the large variations at 6 cm could still indicate that these features undergo large structural changes on timescales of only a few years or perhaps even shorter.

To verify that our 2-D Gaussian fits to the radio images produced accurate total flux density values, we fitted uniform disks to the calibrated visibilities. We found that all flux density values produced using this method were in good agreement with the values plotted in Figure 1.15. Fitting disks to the measured visibilities was a method used by Lim *et al.* (1998) to quantify not only the total flux, but also the area of the region where the radio emission is emanating from. Knowing this area, the brightness temperature (and thus the electron temperature) can be calculated using Equation ???. We followed the same method and applied this equation to our VLA-Pie Town data. The derived electron temperature as a function of distance from the star is plotted in Figure 1.16 along with the values from Lim *et al.* (1998) and the single value from Richards *et al.* (2013) (which was derived by fitting a 2-D ellipse to the low resolution e-MERLIN data set and finding the area of the Gaussian). Although there appears to be some variability in the mean electron temperature at various epoches, our values are consistent with a relatively low temperature wind, which was one of the main findings of Lim *et al.* (1998).

1.15 0.7 cm VLA-Pie Town Maps

All the VLA-Pie Town data were imaged using uniform weighting where each unit of area in the $u - v$ plane is given the same weight irrespective of the number of visibility measurements it contains. The 0.7 cm (i.e., Q band) maps are presented in Figure 1.17 and were the only maps to show significant asymmetric structure in them. The 2004 and 2003 data contain two and three distinct unresolved features respectively, all separated from each other by only ~ 40 mas. The elongated restoring beam in the 2000 data set makes it difficult to detect any distinct

1.16 VLA, VLA-Pie, e-MERLIN: Putting it all together

features in the north south direction although asymmetries are clearly present at a high level of significance. Finally the 1998 data set which does not contain the Pie Town link but has a very circular restoring beam once again looks highly asymmetric but in a different direction to the other epochs.

These high resolution data sets indicate dramatic changes in the radio emitting topology over a time period of only one to two years. The relatively small separation of the distinct unresolved features indicate that they are probably located in the lower chromosphere and may be formed by the large scale convective features believed to exist on the photospheric surface of all red supergiants (Schwarzschild, 1975). In fact, using optical interferometry, such features have been confirmed to exist on the surface of Betelgeuse (e.g., Buscher *et al.*, 1990; Chiavassa *et al.*, 2010; Tuthill *et al.*, 1997; Wilson *et al.*, 1992). Stothers & Leung (1971) believed that the long period brightness variation of 2100 days present in Betelgeuse's optical continuum emission were related to the giant convection cell turnover time. However, Schwarzschild (1975) claimed that their evolution may be as short as 200 days and optical observations appear to agree with this (Tuthill *et al.*, 1997). These timescales would then be consistent with our findings. What we may actually be observing at 0.7 cm is the convective overshoot of these convection cells into an overall weakly ionized atmosphere (Gray, 2008; Josselin & Plez, 2007) releasing the hotter more ionized plasma which radio observations are sensitive to. The changes in the radio emitting topology, caused by this convection cell overshoot, may then be the source of the radio flux variability at Q band at least.

1.16 VLA, VLA-Pie, e-MERLIN: Putting it all together

Our VLA-Pie Town data are in good agreement with the findings of Lim *et al.* (1998). We find that the mean electron temperature falls from a value of ~ 3000 K at $\sim 2 R_\star$ to 1500 K at $\sim 6 R_\star$. Our 0.7 cm radio maps show even more dramatic asymmetries than those seen by Lim *et al.* (1998) due to our superior spatial resolution. These asymmetries change dramatically on timescales as short as

1.16 VLA, VLA-Pie, e-MERLIN: Putting it all together

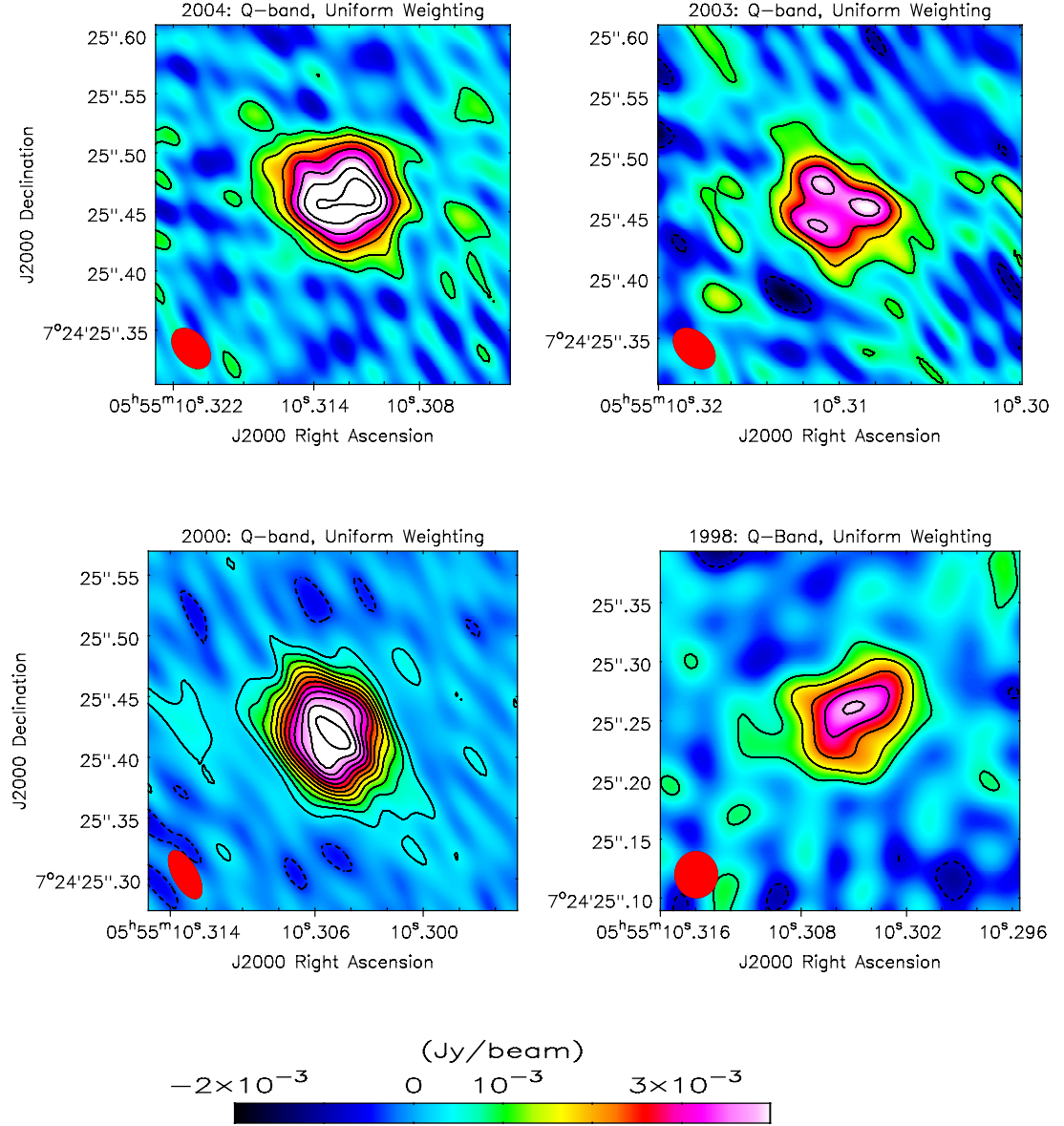


Figure 1.17: High resolution Q band images of Betelgeuse spanning six years. Asymmetries in the inner atmosphere are clearly present in all images. Image contours are set at $(2, 4, 6, \dots, 24) \times \sigma_{rms}$ where $\sigma_{rms} = 0.35, 0.46, 0.18$, and 0.38 mJy for the 2004, 2003, 2000, and 1998 data respectively. The restoring beam is shown in red at the bottom left corner of each image. The 1998 data does not contain the Pie Town link and thus has a more circular restoring beam. The color scheme in all images have the same scaling, i.e., between -2 and $+4 \text{ mJy}$. Each image represents $300 \times 300 \text{ mas}^2$ in area.

1.16 VLA, VLA-Pie, e-MERLIN: Putting it all together

~ 1 yr (and possibly shorter), suggesting a highly dynamic inner atmosphere probably related to large scale surface convection.

The recent e-MERLIN findings of two unresolved *hotspots* separated by 90 mas (i.e., $4 R_\star$) are difficult to explain by referring to our VLA-Pie Town data. Surprisingly, we find no evidence for these features at any wavelengths in our data sets. There are two ways to account for this. The first is that these features are highly time variable and were not as extended, or maybe not even present, when our VLA-Pie Town measurements were taken. The other alternative is that these features are optically thin at the high frequencies where we should have sufficient spatial resolution to resolve them.

Since the majority of the radio flux at 6 cm, is contained within two compact features, it is worth asking the question: “what does the electron temperature profile plotted in Figure 1.16 represent?”. e-MERLIN has shown that at 6 cm at least, the values representing the wind temperature found by Lim *et al.* (1998) are not a true representation of the actual values. If such hotspots were present at higher frequencies again, then we could make the same conclusion about the inaccuracy of the temperature profile throughout the inner atmosphere. This would have major consequences for the theory of mass-loss in Betelgeuse (and M supergiants in general) as the conclusion of Lim *et al.* (1998) was that magnetic waves, acoustic waves, and pulsations all required higher atmospheric temperatures than those found, and were thus not the source of Betelgeuse’s mass-loss. High resolution, multi-wavelength, multi-epoch observations will finally help solve the puzzle as to what is driving betelgeuse’s mass-loss.

A

List of Abbreviations Used in this Thesis.

Table A.1: List of Abbreviations

Acronym	Meaning
ALMA	The Atacama Large Millimeter/submillimeter Array
AGB	Asymptotic Giant Branch
ALC	Automatic Level Control
BIMA	Berkeley Illinois Maryland Association
CARMA	Combined Array for Research in Millimeter-wave Astronomy
CASA	Common Astronomy Software Application
CSE	Circumstellar Envelope
DDT	Director's Discretionary Time
e-MERLIN	e-Multi-Element Radio Linked Interferometer Network
FFT	Fast Fourier Transform
FITS	Flexible Image Transport System
FOV	Field of View
GBT	Robert C. Byrd Green Bank Telescope
GHRS	Goddard High-Resolution Spectrograph
GREAT	German Receiver for Astronomy at Terahertz Frequencies
HIFI	Heterodyne Instrument for the Far Infrared
HPBW	Half Power Beamwidth
H-R	Hertzsprung-Russell

Continued on next page

Table A.1 – *Continued from previous page*

Acronym	Meaning
HST	Hubble Space Telescope
IF	Intermediate Frequency
IOTA	Infrared Optical Telescope Array
IR	Infrared
IRAM	Institut de Radioastronomie Millimétrique
ISM	Interstellar Medium
IUE	International Ultraviolet Explorer
LNA	Low Noise Amplifier
LO	Local Oscillator
LSR	Local Standard of Rest
LTE	Local Thermodynamic Equilibrium
MEM	Maximum Entropy Method
MERLIN	Multi-Element Radio Linked Interferometer Network
MHD	Magnetohydrodynamic
OVRO	Owens Valley Radio Observatory
OSRO	Open Shared Risk Observing
RF	Radio Frequency
RFI	Radio Frequency Interference
RGC	Red Giant Clump
RGB	Red Giant Branch
RSG	Red Supergiant
S/N	signal-to-noise ratio
SB	Scheduling Block
SGB	Subgiant Branch
SOFIA	Stratospheric Observatory for Infrared Astronomy
SMA	Submillimeter Array
SZA	Sunyaev-Zel'dovich Array
SIS	Superconductor Insulator Superconductor
UV	Ultraviolet
VLA	Karl G. Jansky Very Large Array
VLBA	Very Long Baseline Array
VLT	Very Large Telescope
W-R	Wolf-Rayet

References

- ALTENHOFF, W.J., THUM, C. & WENDKER, H.J. (1994). Radio emission from stars: A survey at 250 GHz. *Astronomy & Astrophysics*, **281**, 161–183. (Cited on page 21.)
- BECKLIN, E.E. & GEHRZ, R.D. (2009). SOFIA: Stratospheric Observatory for Infrared Astronomy. In D. C. Lis, J. E. Vaillancourt, P. F. Goldsmith, T. A. Bell, N. Z. Scoville, & J. Zmuidzinas, ed., *Submillimeter Astrophysics and Technology: a Symposium Honoring Thomas G. Phillips*, vol. 417 of *Astronomical Society of the Pacific Conference Series*, 101. (Cited on page 21.)
- BERNAT, A.P., HALL, D.N.B., HINKLE, K.H. & RIDGWAY, S.T. (1979). Observations of CO circumstellar absorption in the 4.6 micron spectrum of Alpha Orionis. *Astrophysical Journal Letters*, **233**, L135–L139. (Cited on pages 3, 4, 13, 24 and 26.)
- BLUNDELL, R. (2007). The Submillimeter Array. In *IEEE MTT-S International Microwave Symposium Digest*, 1857–1860. (Cited on page 21.)
- BOOKBINDER, J.A., STENCEL, R.E., DRAKE, S.A., SIMON, T., LINSKY, J.L. & FLORKOWSKI, D. (1987). VLA Observations of Rapid 6 cm Flux Variations in α Ori. In J. L. Linsky & R. E. Stencel, ed., *Cool Stars, Stellar Systems and the Sun*, vol. 291 of *Lecture Notes in Physics*, Berlin Springer Verlag, 337. (Cited on pages 20, 34 and 35.)
- BOOTHROYD, A.I. & SACKMANN, I.J. (1999). The CNO Isotopes: Deep Circulation in Red Giants and First and Second Dredge-up. *Astrophysical Journal*, **510**, 232–250. (Cited on page 3.)
- BOTTLINGER, C.F. (1911). Die Bahn des spektroskopischen Doppelsternes α Orionis. *Astronomische Nachrichten*, **187**, 33. (Cited on page 6.)
- BRACEWELL, R.N. (2000). *The Fourier Transform and Its Applications*. Columbus, OH: McGraw Hill, 3rd edn. (Cited on page 18.)
- BUSCHER, D.F., BALDWIN, J.E., WARNER, P.J. & HANIFF, C.A. (1990). Detection of a bright feature on the surface of Betelgeuse. *Monthly Notices of the Royal Astronomical Society*, **245**, 7P–11P. (Cited on page 38.)
- CARPENTER, K.G. & ROBINSON, R.D. (1997). GHRS Observations of Cool, Low-Gravity Stars. III. Plasma Flows and Turbulence in the Outer Atmosphere of alpha Orionis (M2 Iab). *Astrophysical Journal*, **479**, 970–+. (Cited on pages 19 and 33.)
- CHARBONNEL, C. (1995). A Consistent Explanation for $^{12}\text{C}/^{13}\text{C}$, ^{7}Li and ^{3}He Anomalies in Red Giant Stars. *Astrophysical Journal Letters*, **453**, L41. (Cited on page 3.)

REFERENCES

- CHIAVASSA, A., HAUBOIS, X., YOUNG, J.S., PLEZ, B., JOSSELIN, E., PERRIN, G. & FREYTAG, B. (2010). Radiative hydrodynamics simulations of red supergiant stars. II. Simulations of convection on Betelgeuse match interferometric observations. *Astronomy & Astrophysics*, **515**, A12. (Cited on page 38.)
- DANCHI, W.C., BESTER, M., DEGIACOMI, C.G., GREENHILL, L.J. & TOWNES, C.H. (1994). Characteristics of dust shells around 13 late-type stars. *Astronomical Journal*, **107**, 1469–1513. (Cited on page 2.)
- DE GRAAUW, T., HELMICH, F.P., PHILLIPS, T.G., STUTZKI, J., CAUX, E., WHYBORN, N.D., DIELEMAN, P., ROELFSEMA, P.R., AARTS, H., ASSENDORP, R., BACHILLER, R., BAECHTOLD, W., BARCIA, A., BEINTEMA, D.A., BELITSKY, V., BENZ, A.O., BIEBER, R., BOOGERT, A., BORYS, C., BUMBLE, B., CAÏS, P., CARIS, M., CERULLI-IRELLI, P., CHATTOPADHYAY, G., CHEREDNICHENKO, S., CIECHANOWICZ, M., COEUR-JOLY, O., COMITO, C., CROS, A., DE JONGE, A., DE LANGE, G., DELFORGES, B., DELORME, Y., DEN BOGGENDE, T., DESBAT, J.M., DIEZ-GONZÁLEZ, C., DI GIORGIO, A.M., DUBBELDAM, L., EDWARDS, K., EGGENS, M., ERICKSON, N., EVERE, J., FICH, M., FINN, T., FRANKE, B., GAIER, T., GAL, C., GAO, J.R., GALLEG, J.D., GAUFFRE, S., GILL, J.J., GLENZ, S., GOLSTEIN, H., GOOLOOZE, H., GUNSING, T., GÜSTEN, R., HARTOGH, P., HATCH, W.A., HIGGINS, R., HONINGH, E.C., HUISMAN, R., JACKSON, B.D., JACOBS, H., JACOBS, K., JARCHOW, C., JAVADI, H., JELLEMA, W., JUSTEN, M., KARPOV, A., KASEMANN, C., KAWAMURA, J., KEIZER, G., KESTER, D., Klapwijk, T.M., KLEIN, T., KOLBERG, E., KOOI, J., KOOIMAN, P.P., KOPF, B., KRAUSE, M., KRIEG, J.M., KRAMER, C., KRUIZENGA, B., KUHN, T., LAUWEN, W., LAI, R., LARSSON, B., LEDUC, H.G., LEINZ, C., LIN, R.H., LISEAU, R., LIU, G.S., LOOSE, A., LÓPEZ-FERNANDEZ, I., LORD, S., LUINGE, W., MARSTON, A., MARTÍN-PINTADO, J., MAESTRINI, A., MAIWALD, F.W., MCCOEY, C., MEHDI, I., MEGEJ, A., MELCHIOR, M., MEINSMA, L., MERKEL, H., MICHALSKA, M., MONSTEIN, C., MORATSCHKE, D., MORRIS, P., MULLER, H., MURPHY, J.A., NABER, A., NATALE, E., NOWOSIELSKI, W., NUZZOLO, F., OLBERG, M., OLBRICH, M., ORFEI, R., ORLEANSKI, P., OSSenkopf, V., PEACOCK, T., PEARSON, J.C., PERON, I., PHILLIP-MAY, S., PIAZZO, L., PLANESAS, P., RATAJ, M., RAVERA, L., RISACHER, C., SALEZ, M., SAMOSKA, L.A., SARACENO, P., SCHIEDER, R., SCHLECHT, E., SCHLÖDER, F., SCHMÜLLING, F., SCHULTZ, M., SCHUSTER, K., SIEBERTZ, O., SMIT, H., SZCZERBA, R., SHIPMAN, R., STEINMETZ, E., STERN, J.A., STOKROOS, M., TEIPEN, R., TEYSSIER, D., TILS, T., TRAPPE, N., VAN BAAREN, C., VAN LEEUWEN, B.J., VAN DE STADT, H., VISSER, H., WILDEMAN, K.J., WAFELBAKKER, C.K., WARD, J.S., WESSELIUS, P., WILD, W., WULFF, S., WUNSCH, H.J., TIELENS, X., ZAAL, P., ZIRATH, H., ZMUIDZINAS, J. & ZWART, F. (2010). The Herschel-Heterodyne Instrument for the Far-Infrared (HIFI). *Astronomy & Astrophysics*, **518**, L6. (Cited on page 21.)
- DRAKE, S.A., BOOKBINDER, J.A., FLORKOWSKI, D.R., LINSKY, J.L., SIMON, T. & STENCEL, R.E. (1992). Four Years of Monitoring a Orionis with the VLA: Where have all the Flares Gone? In M. S. Giampapa & J. A. Bookbinder, ed., *Cool Stars, Stellar Systems, and the Sun*, vol. 26 of *Astronomical Society of the Pacific Conference Series*, 455. (Cited on pages 20, 34 and 35.)
- DUPREE, A.K., BALIUNAS, S.L., HARTMANN, L., GUINAN, E.F. & SONNEBORN, G. (1990). Alpha ORI - Evidence for pulsation. In C. Cacciari & G. Clementini, eds., *Confrontation Between Stellar Pulsation and Evolution*, vol. 11 of *Astronomical Society of the Pacific Conference Series*, 468–471. (Cited on page 5.)

REFERENCES

- EGGLETON, P.P., DEARBORN, D.S.P. & LATTANZIO, J.C. (2007). Compulsory Deep Mixing of ^3He and CNO Isotopes on the First Giant Branch. In R.J. Stancliffe, G. Houdek, R.G. Martin & C.A. Tout, eds., *Unsolved Problems in Stellar Physics: A Conference in Honor of Douglas Gough*, vol. 948 of *American Institute of Physics Conference Series*, 27–34. (Cited on page 3.)
- FAMAÉY, B., JORISSEN, A., LURI, X., MAYOR, M., UDRY, S., DEJONGHE, H. & TURON, C. (2005). Local kinematics of K and M giants from CORAVEL/Hipparcos/Tycho-2 data. Revisiting the concept of superclusters. *Astronomy & Astrophysics*, **430**, 165–186. (Cited on page 9.)
- GILLILAND, R.L. & DUPREE, A.K. (1996). First Image of the Surface of a Star with the Hubble Space Telescope. *Astrophysical Journal Letters*, **463**, L29. (Cited on page 27.)
- GOLDBERG, L. (1984). The variability of alpha Orionis. *Publications of the Astronomical Society of the Pacific*, **96**, 366–371. (Cited on pages 6 and 19.)
- GOLDBERG, L., RAMSEY, L., TESTERMAN, L. & CARBON, D. (1975). High-resolution profiles of sodium and potassium lines in alpha Orionis. *Astrophysical Journal*, **199**, 427–431. (Cited on page 4.)
- GRAY, D.F. (2008). Mass Motions in the Photosphere of Betelgeuse. *Astronomical Journal*, **135**, 1450–1458. (Cited on page 38.)
- GUESTEN, R., HARTOGH, P., HUEBERS, H.W., GRAF, U.U., JACOBS, K., ROESER, H.P., SCHAEFER, F., SCHIEDER, R.T., STARK, R., STUTZKI, J., VAN DER WAL, P. & WUNSCH, A. (2000). GREAT: the first-generation German heterodyne receiver for SOFIA. In R. K. Melugin & H.-P. Röser, ed., *Society of Photo-Optical Instrumentation Engineers (SPIE) Conference Series*, vol. 4014, 23–30. (Cited on page 21.)
- HARPER, G.M. (2013). Atmospheric structure and dynamics: the spatial and temporal domains. In P. Kervella, T. Le Bertre & G. Perrin, eds., *EAS Publications Series*, vol. 60 of *EAS Publications Series*, 59–68. (Cited on page 26.)
- HARPER, G.M., BROWN, A. & LIM, J. (2001). A Spatially Resolved, Semiempirical Model for the Extended Atmosphere of α Orionis (M2 Iab). *Astrophysical Journal*, **551**, 1073–1098. (Cited on pages 2, 28, 30, 31, 32 and 35.)
- HARPER, G.M., BROWN, A. & GUINAN, E.F. (2008). A New VLA-Hipparcos Distance to Betelgeuse and its Implications. *Astronomical Journal*, **135**, 1430–1440. (Cited on pages 6, 10, 29 and 33.)
- HARRIS, M.J. & LAMBERT, D.L. (1984). Oxygen isotopes in the atmospheres of Betelgeuse and Antares. *Astrophysical Journal*, **281**, 739–745. (Cited on page 3.)
- HARTMANN, L. & AVRETT, E.H. (1984). On the extended chromosphere of Alpha Orionis. *Astrophysical Journal*, **284**, 238–249. (Cited on page 27.)
- HINKLE, K.H., LAMBERT, D.L. & SNELL, R.L. (1976). The C-12/C-13 ratio in stellar atmospheres. VI - Five luminous cool stars. *Astrophysical Journal*, **210**, 684–693. (Cited on page 3.)

REFERENCES

- HUGGINS, P.J. (1987). CO in the circumstellar envelope of Alpha Orionis. *Astrophysical Journal*, **313**, 400–407. (Cited on pages 4, 8, 9 and 13.)
- HUGGINS, P.J., BACHILLER, R., COX, P. & FORVEILLE, T. (1994). Neutral carbon in the circumstellar envelope of alpha Orionis. *Astrophysical Journal Letters*, **424**, L127–L130. (Cited on pages 4, 5, 12 and 13.)
- JOSSELIN, E. & PLEZ, B. (2007). Atmospheric dynamics and the mass loss process in red supergiant stars. *Astronomy & Astrophysics*, **469**, 671–680. (Cited on page 38.)
- KALER, J.B., IBEN, I., JR. & BECKER, S.A. (1978). On the enhancement of helium and nitrogen in planetary nebulae. *Astrophysical Journal Letters*, **224**, L63–L66. (Cited on page 3.)
- KERVELLA, P., PERRIN, G., CHIAVASSA, A., RIDGWAY, S.T., CAMI, J., HAUBOIS, X. & VERHOELST, T. (2011). The close circumstellar environment of Betelgeuse. II. Diffraction-limited spectro-imaging from 7.76 to 19.50 μ m with VLT/VISIR. *Astronomy & Astrophysics*, **531**, A117. (Cited on page 18.)
- KNAPP, G.R. & MORRIS, M. (1985). Mass loss from evolved stars. III - Mass loss rates for fifty stars from CO J = 1-0 observations. *Astrophysical Journal*, **292**, 640–669. (Cited on page 4.)
- KNAPP, G.R., PHILLIPS, T.G. & HUGGINS, P.J. (1980). Detection of CO Emission at 1.3-MILLIMETERS from the Betelgeuse Circumstellar Shell. *Astrophysical Journal Letters*, **242**, L25+. (Cited on pages 4, 9 and 13.)
- LAMB, S.A., IBEN, I., JR. & HOWARD, W.M. (1976). On the evolution of massive stars through the core carbon-burning phase. *Astrophysical Journal*, **207**, 209–232. (Cited on page 2.)
- LAMBERT, D.L. & VANDEN BOUT, P.A. (1978). Constraints on the properties of circumstellar shells from observations of thermal CO and SiO millimeter line emission. *Astrophysical Journal*, **221**, 854–860. (Cited on page 25.)
- LAMBERT, D.L., DEARBORN, D.S. & SNEDEN, C. (1974). The C-12/C-13 ratio in stellar atmospheres. II - CN and CO in alpha Orionis. *Astrophysical Journal*, **193**, 621–630. (Cited on page 3.)
- LAMBERT, D.L., BROWN, J.A., HINKLE, K.H. & JOHNSON, H.R. (1984). Carbon, nitrogen, and oxygen abundances in Betelgeuse. *Astrophysical Journal*, **284**, 223–237. (Cited on page 2.)
- LEVESQUE, E.M., MASSEY, P., OLSEN, K.A.G., PLEZ, B., JOSSELIN, E., MAEDER, A. & MEYNET, G. (2005). The Effective Temperature Scale of Galactic Red Supergiants: Cool, but Not As Cool As We Thought. *Astrophysical Journal*, **628**, 973–985. (Cited on page 29.)
- LIM, J., CARILLI, C.L., WHITE, S.M., BEASLEY, A.J. & MARSON, R.G. (1998). Large convection cells as the source of Betelgeuse's extended atmosphere. *Nature*, **392**, 575–577. (Cited on pages 19, 27, 28, 30, 34, 37, 38 and 40.)

REFERENCES

- MEYNET, G. & MAEDER, A. (2003). Stellar evolution with rotation. X. Wolf-Rayet star populations at solar metallicity. *Astronomy & Astrophysics*, **404**, 975–990. (Cited on page 10.)
- MUXLOW, T.W.B. (2003). e-MERLIN - a Real-Time VLBI Array. In Y.C. Minh, ed., *New technologies in VLBI*, vol. 306 of *Astronomical Society of the Pacific Conference Series*, 245. (Cited on page 27.)
- NEWELL, R.T. & HJELLMING, R.M. (1982). Radio emission from the extended chromosphere of Alpha Orionis. *Astrophysical Journal Letters*, **263**, L85–L87. (Cited on pages 27, 34 and 36.)
- O'GORMAN, E., HARPER, G.M., BROWN, J.M., BROWN, A., REDFIELD, S., RICHTER, M.J. & REQUENA-TORRES, M.A. (2012). CARMA CO($J = 2 - 1$) Observations of the Circumstellar Envelope of Betelgeuse. *Astronomical Journal*, **144**, 36. (Cited on page 1.)
- PAVLENKO, Y.V., JONES, H.R.A. & LONGMORE, A.J. (2003). Carbon abundances and $^{12}\text{C}/^{13}\text{C}$ from globular cluster giants. *Monthly Notices of the Royal Astronomical Society*, **345**, 311–324. (Cited on page 3.)
- PILBRATT, G.L., RIEDINGER, J.R., PASSVOGEL, T., CRONE, G., DOYLE, D., GAGEUR, U., HERAS, A.M., JEWELL, C., METCALFE, L., OTT, S. & SCHMIDT, M. (2010). Herschel Space Observatory. An ESA facility for far-infrared and submillimetre astronomy. *Astronomy & Astrophysics*, **518**, L1. (Cited on page 22.)
- PLEZ, B. & LAMBERT, D.L. (2002). The outer atmosphere of the M-type supergiant alpha Orionis: K I 7699 Åemission. *Astronomy & Astrophysics*, **386**, 1009–1018. (Cited on pages 18 and 26.)
- RICHARDS, A.M.S., DAVIS, R.J., DECIN, L., ETOKA, S., HARPER, G.M., LIM, J.J., GARRINGTON, S.T., GRAY, M.D., McDONALD, I., O'GORMAN, E. & WITTKOWSKI, M. (2013). e-MERLIN resolves Betelgeuse at λ 5 cm: hotspots at 5 R. *Monthly Notices of the Royal Astronomical Society*, **432**, L61. (Cited on pages 1, 27, 29, 30, 34, 36 and 37.)
- SAHA, S.K. (2011). *Aperture Synthesis*. (Cited on page 29.)
- SANFORD, R.F. (1933). No. 464. The variation in the radial velocity of alpha Orionis from 1923 to 1931. *Contributions from the Mount Wilson Observatory / Carnegie Institution of Washington*, **464**, 1–10. (Cited on pages 5 and 6.)
- SCHWARZSCHILD, M. (1975). On the scale of photospheric convection in red giants and supergiants. *Astrophysical Journal*, **195**, 137–144. (Cited on page 38.)
- SKINNER, C.J., DOUGHERTY, S.M., MEIXNER, M., BODE, M.F., DAVIS, R.J., DRAKE, S.A., ARENS, J.F. & JERNIGAN, J.G. (1997). Circumstellar environments - V. The asymmetric chromosphere and dust shell of alpha Orionis. *Monthly Notices of the Royal Astronomical Society*, **288**, 295–306. (Cited on page 27.)
- SMITH, M.A., PATTEN, B.M. & GOLDBERG, L. (1989). Radial-velocity variations in Alpha Ori, Alpha Sco, and Alpha HER. *Astronomical Journal*, **98**, 2233–2248. (Cited on page 5.)

REFERENCES

- SMITH, N., HINKLE, K.H. & RYDE, N. (2009). Red Supergiants as Potential Type IIn Supernova Progenitors: Spatially Resolved 4.6 μ m CO Emission Around VY CMa and Betelgeuse. *Astronomical Journal*, **137**, 3558–3573. (Cited on page 18.)
- SPENCER JONES, H. (1928). The radial velocity variations of a Orionis and a Scorpii. *Monthly Notices of the Royal Astronomical Society*, **88**, 660. (Cited on pages 5 and 6.)
- SPINRAD, H. & VARDYA, M.S. (1966). Approximate Abundances of the Light Elements from the Molecular Spectra of M and S Stars. *Astrophysical Journal*, **146**, 399. (Cited on page 2.)
- STEBBINS, J. & HUFFER, C.M. (1931). Photo-electric studies of five variable stars. *Publications of the Washburn Observatory*, **15**, 178–213. (Cited on page 5.)
- STOTHERS, R. & LEUNG, K.C. (1971). Luminosities, masses and periodicities of massive red supergiants. *Astronomy & Astrophysics*, **10**, 290–300. (Cited on pages 5 and 38.)
- TSUJI, T. (1979). A probe of optically thin dust shells around late-type stars. *Publications of the Astronomical Society of Japan*, **31**, 43–60. (Cited on page 4.)
- TUTHILL, P.G., HANIFF, C.A. & BALDWIN, J.E. (1997). Hotspots on late-type supergiants. *Monthly Notices of the Royal Astronomical Society*, **285**, 529–539. (Cited on page 38.)
- WEYMANN, R. (1962). Physical Conditions in the Circumstellar Envelope of α Orionis. *Astrophysical Journal*, **136**, 844–+. (Cited on pages 4 and 6.)
- WILSON, R.W., BALDWIN, J.E., BUSCHER, D.F. & WARNER, P.J. (1992). High-resolution imaging of Betelgeuse and Mira. *Monthly Notices of the Royal Astronomical Society*, **257**, 369–376. (Cited on page 38.)